CHARACTERIZATION OF MWIR QUANTUM WELL INFRARED PHOTODETECTOR IMAGING SENSOR ARRAYS ON INP SUBSTRATES

A THESIS SUBMITTED TO
THE GRADUATE SCHOOL OF NATURAL AND APPLIED SCIENCES
OF
MIDDLE EAST TECHNICAL UNIVERSITY

BY

ONUR TANIŞ

IN PARTIAL FULFILLMENT OF THE REQUIREMENTS
FOR
THE DEGREE OF MASTER OF SCIENCE
IN
ELECTRICAL AND ELECTRONICS ENGINEERING

SEPTEMBER 2023

Approval of the thesis:

CHARACTERIZATION OF MWIR QUANTUM WELL INFRARED PHOTODETECTORS IMAGING SENSOR ARRAYS ON INP SUBSTRATES

submitted by **ONUR TANIŞ** in partial fulfillment of the requirements for the degree of **Master of Science** i**n Electrical and Electronics Engineering, Middle East Technical University** by,

Prof. Dr. Halil Kalıpçılar
Dean, Graduate School of **Natural and Applied Sciences** _____

Prof. Dr. İlkay Ulusoy
Head of Department, **Electrical and Electronics Engineering** _____

Prof. Dr. Cengiz Beşikci
Supervisor, **Electrical and Electronics Engineering, METU** _____

Examining Committee Members:

Prof. Dr. Haluk Külah
Electrical and Electronics Engineering, METU _____

Prof. Dr. Cengiz Beşikci
Electrical and Electronics Engineering, METU _____

Prof. Dr. Mehmet Ünlü
Electrical and Electronics Engineering, TOBB ETU _____

Date: 07.09.2023

I hereby declare that all information in this document has been obtained and presented in accordance with academic rules and ethical conduct. I also declare that, as required by these rules and conduct, I have fully cited and referenced all material and results that are not original to this work.

Name, Surname: Onur Tanış

Signature :

ABSTRACT

CHARACTERIZATION OF MWIR QUANTUM WELL INFRARED PHOTODETECTORS IMAGING SENSOR ARRAYS ON INP SUBSTRATES

Tanış, Onur
Master of Science, Electrical and Electronics Engineering
Supervisor: Prof. Dr. Cengiz Beşikci

September 2023, 85 pages

QWIP (Quantum Well Infrared Photodetector) technology has been researched for over 30 years to create a strong alternative to low bandgap material-based IR (Infrared) technologies. However, low conversion efficiency of QWIPs based on standard material system has delayed the actual potential of this technology. The emergence of the InP based QWIP FPAs (Focal Plane Arrays) has great potential to make QWIP technology attractive again. InP/$In_xGa_{1-x}As$ based QWIP FPAs with high indium mole fraction can reach conversion efficiency as high as 70% in the MWIR (Mid-wave Infrared) band with the ability of sensing of normal radiation which allows utilization of high performance QWIP based FPAs for low background and high-speed applications. In other respects, an FPA must have extra qualifications. Today's new generation FPAs need new features. These can be categorized as very high uniformity, operability, stability, correctability, scalability, and manufacturability with low pitch. In the scope of the thesis work, InP/$In_{0.85}Ga_{0.15}As$ and InP/InAs based diffraction-grating free QWIP FPAs with 640x512 format and 15 μm pitch were characterized. InP/$In_{0.85}Ga_{0.15}As$ based FPA exhibited mean NETD (Noise Equivalent Temperature Difference) of 20.2 mK at 20

ms integration time and InP/InAs based FPA demonstrated 27.8 mK NETD at 10 ms integration time. Although both designs have strained lattice structure, FPAs yielded very high uniformity. The absence of the optical coupler removes a challenging fabrication step. Mature fabrication processes of the III-V material system ease the production. Widely accessible InP substrates make this technology affordable and reachable.

Keywords: QWIP, FPA, MWIR, infrared, InP

ÖZ

INP TABAN ÜZERİNDE MWIR KUANTUM KUYULU KIZILÖTESİ FOTODEDEKTÖR GÖRÜNTÜLEME SENSÖRLERİNİN KARAKTERİZASYONU

Tanış, Onur
Yüksek Lisans, Elektrik ve Elektronik Mühendisliği
Tez Yöneticisi: Prof. Dr. Cengiz Beşikci

Eylül 2023, 85 sayfa

Kuantum kuyulu kızılötesi fotodetektör (KKKF) teknolojisi otuz yılı aşkın süredir düşük bant aralıklı yarı iletken malzemesine dayanan kızılötesi detektör teknolojilerine alternatif oluşturmak için araştırılmaktadır. Fakat, standart materyal sistemine dayanan KKKF'ler bu teknolojinin gerçek potansiyelini geciktirmiştir. InP materyal sistemi tabanlı KKKF odak düzlem matrislerini (ODK) ortaya çıkması KKKF teknolojisini yeniden ilgi çekici duruma getirmek için büyük potansiyele sahiptir. Orta dalga boyu kızılötesi (ODBK) bandında kullanılan yüksek indiyum mol oranına sahip InP/$In_xGa_{1-x}As$ tabanlı KKKF ODK'ler dik düşen radyasyonu algılama yeteneği olduğundan %70 dönüşüm verimliliğine ulaşabilirler ve düşük ışık ortamı ve yüksek kare sayısı ihtiyacı olan uygulamalarda kullanılabilirler. Bunun yanı sıra, günümüzde yeni nesil ODK'lerde ek yeni özelliklere de ihtiyaç duyulmaktadır. Bunlar düşük piksel adımıyla beraber çok yüksek tekdüzelik, çalışabilirlik, kararlılık, düzeltilebilirlik, ölçeklenebilirlik ve üretilebilirlik olarak kategorize edilebilir. Bu tez çalışması kapsamında kırınım ızgarası olmayan InP/$In_{0.85}Ga_{0.15}As$ ve InP/InAs tabanlı 640x512 formatına ve 15 μm piksel adımına sahip KKKF ODK'ler karakterize edilmiştir. InP/$In_{0.85}Ga_{0.15}As$ tabanlı ODK 20 ms

entegrasyon zamanıyla ortalama 20.2 mK gürültü eşdeğer sıcaklık farkına (GESF) ve InP/InAs tabanlı ODK 10 ms entegrasyon zamanıyla ortalama 27.8 mK gürültü eşdeğer sıcaklık farkına denk performans gösterdiler. Her iki tasarım da gergin örgü yapısına sahip olmasına rağmen ODK'ler yüksek tekdüzelik sundular. Optik bağlaştırıcının olmayışı, zorlayıcı bir üretim adımını ortadan kaldırmaktadır. III-V malzeme sistemlerinin olgun fabrikasyon adımları, KKKF ODK'lerin üretimi kolaylaştırmaktadır. Kolay erişebilir InP alttaşlar ise üretim maliyetini kolay karşılanabilir ve ulaşılabilir hale getirmektedir.

Anahtar Kelimeler: KKKF, ODK, ODBK, kızılötesi, InP

To curious minds

ACKNOWLEDGMENTS

First, I would like to express my gratitude to my advisor Prof. Dr. Cengiz Beşikci, for his invaluable guidance and supervision. This thesis would not have been possible without his encouragement and support.

I would like to express my gratitude to Prof. Dr. Haluk Külah and Prof. Dr. Mehmet Ünlü for their willingness to serve on my thesis committee.

I would like to thank Saadettin Veysel Balcı and Oğuz Onur Güngör for their help in all the laboratory work and for their friendship.

I want to express my gratitude to the past members of the laboratory for their contributions to laboratory knowledge.

I want to take a moment to thank my friends Yahya Can Tuğrul, Furkan Aldemir, Işılay Kolan and Hakan Keskin for their support in all aspects of life. Your friendship means the world to me, and I'm grateful for your constant encouragement and presence.

Last but not least, I want to express my deepest gratitude to my family. Their unwavering support, love, and encouragement. I am profoundly thankful for their sacrifices and understanding.

TABLE OF CONTENTS

LIST OF TABLES

TABLES

LIST OF FIGURES

FIGURES

CHAPTER 1

INTRODUCTION

Electromagnetic radiation having wavelengths between wavelength of visible light and radio waves is called Infrared Radiation (IR). Typically, it covers the region between 0.7 μm and 100 μm and is invisible to the human eye. Yet, this does not mean that IR is insensible by humans. Human skin can sense the heat increase due to IR. The first observation of IR was in 1681. E. Mariotte realized that the visible part of sunlight falling on glass can pass through it [1]. However, the transmission of the heat, IR, was blocked by the glass and an object behind the glass did not warm up [1]. The observation is also known as the greenhouse effect [1]. In 1800, W. Herschel demonstrated an experiment by falling light on a thermometer [2]. He passed the sunlight through a prism and realized that beyond red light, even though there was not any visible radiation, an unforeseen increase in thermometer reading occurred [2]. The experiment revealed the presence of invisible radiation, infrared [2]. After the discovery of IR, many efforts have been made to detect it. In 1821 T. J. Seeback showed the effect of thermoelectricity and presented the first thermocouple [3]. The first bolometer which is based on resistance change in the case of incident IR was developed by Langley in 1880 [3]. He observed solar irradiation and measured its intensity at different wavelengths [3]. Up to the 20^{th} century, thermal detectors had been used to sense IR [3].

In order to increase the sensitivity further, the first photon detector was developed in 1917 by T.W. Case. He observed that a material based on sulfur and thallium exhibited photoconductivity to IR but unstable resistance, high noise characteristics, and loss of responsivity in the case of high exposure to light were weaknesses of this

type of detector [3]. In 1930, lead sulfide (PbS) photoconductive detectors having a response between 1.5 μm and 3.0 μm was developed by E.W. Kutzscher [3]. These detectors were thin films fabricated with evaporation techniques [3]. More sensitive Pb-based detectors such as lead selenide (PbSe) and lead telluride (PbTe) were developed in 1944 [3]. The usage of narrow-bandgap semiconductors like indium antimonide (InSb) and mercury cadmium telluride (HgCdTe) enhanced IR detection further [3]. Numerous photodetectors have been fabricated with InSb and HgCdTe technologies. However, design restrictions of InSb, the production difficulties of HgCdTe and the high cost stimulated the development of III-V larger bandgap-based photodetectors. Quantum Well Infrared Detectors (QWIPs) have been researched since 1987 [4]. Today, QWIP technology is considered as an inexpensive alternative to other low bandgap IR technologies thanks to low-cost substrates and mature fabrication techniques of III-V material systems. Robustness and stability over time and outstanding uniformity, make them one of the effective members of the IR detector family both for single-pixel and focal plane array (FPA) applications.

1.1 Infrared Radiation Fundamentals

1.1.1 Blackbody Radiation

If an object has a temperature above absolute zero Kelvin, it emits electromagnetic radiation. The amount of radiated power and spectral density of the radiation depends on the object's temperature and emissivity and higher object temperature results in a larger amount of radiant power. The energy of a photon in emitted radiation depends on its wavelength and the relationship is given by [5]:

$$E = \frac{hc}{\lambda} \tag{1.1}$$

where E is the energy of the photon, λ is the wavelength of the photon, h is Planck's constant, and c is the speed of light.

Radiation incident on a substance is absorbed in the form of energy, reflected at the surface, or transmitted through it. The probability of each case is characterized by coefficients. These are absorbance (α), reflectance (ρ), and transmittance (T). In order to maintain the conservation of energy, the summation of all these coefficients must be equal to 1 [5]

$$T + \rho + \alpha = 1 \tag{1.2}$$

Absorbed power must be also emitted to maintain the thermal equilibrium of the object. Kirchhoff's law of thermal radiation states that under thermal equilibrium, emitted power by an object is equal to absorbed power [6]. It can be expressed as:

$$\varepsilon(\lambda, T) = \alpha(\lambda, T) \tag{1.3}$$

where ε is the emissivity, λ is the wavelength and T is the temperature of the object [6]. Emissivity is the measure of how well an object radiates its energy as thermal radiation. Its value must be between 0 and 1. A high emissivity value indicates that the object is a good emitter. Mathematically, it is the ratio of the total exitance of an object to a blackbody source at the same temperature

$$\varepsilon = \frac{M_{Object}}{M_{Blackbody}} \tag{1.4}$$

A blackbody is an idealized object that absorbs all incident electromagnetic radiation without reflecting and transmitting. Therefore, the coefficient of emissivity is equal to 1. The emission spectrum of a perfect blackbody is characterized by Planck's formula given by

$$M_\lambda(\lambda, T) = \frac{2\pi hc^2}{\lambda^5(e^{\frac{hc}{\lambda k_b T}} - 1)} \tag{1.5}$$

where M_λ is the spectral exitance and k_b is the Boltzmann constant [5].

As seen from Figure 1.1 Planck's formula indicates two important outcomes. The total radiant power increases and peak wavelength of spectral exitance decreases with increasing blackbody temperature.

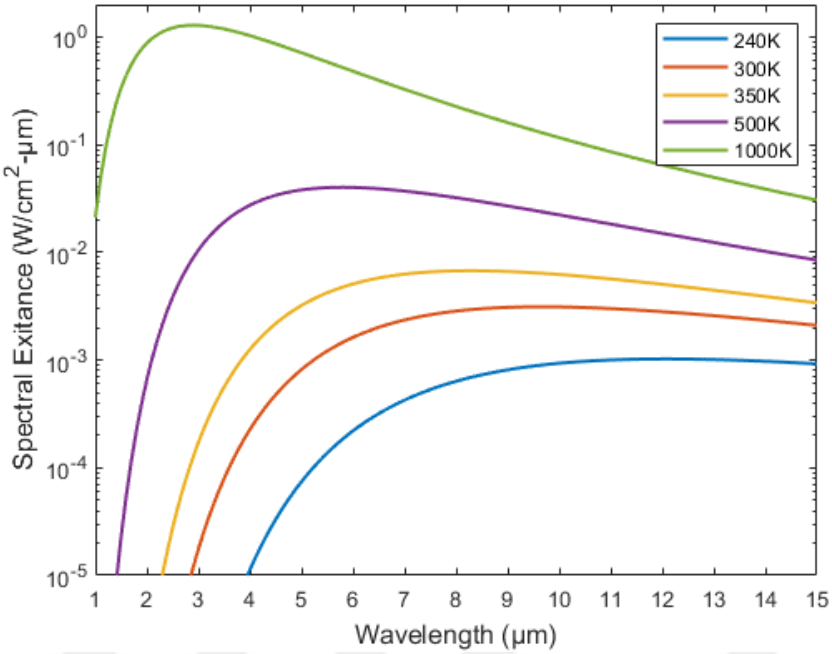

Figure 1.1 Spectral exitance values for different blackbody temperatures

The amount of total radiant power per unit area emitted by a blackbody can be calculated by integrating Equation (1.5) over wavelength

$$M = \int_0^\infty M_\lambda(\lambda, T)d\lambda = \sigma T^4 \tag{1.6}$$

where σ is the Stefan-Boltzmann constant [5]. By solving the equation of derivative of Planck's law with respect to wavelength and equating to zero, peak spectral exitance wavelength for a specific temperature can be found

$$\frac{\partial M_\lambda}{\partial \lambda} = 0 \tag{1.7}.$$

The solution is the Wien's Displacement Law [5]

$$\lambda_{peak} T = 2898\ \mu m.K \qquad (1.8).$$

Table 1.1 shows some results for different blackbody temperatures.

Table 1.1 Peak spectral exitance wavelength for different blackbody temperatures

Temperature	Peak Spectral Exitance Wavelength
273 K	10.62 μm
300 K	9.66 μm
310 K	9.35 μm
5700 K	0.51 μm

As seen in Table 1.1 human body emits radiation around 9 μm. In order to apply thermal imaging of human body, photodetectors must operate around these wavelengths.

1.1.2 Atmospheric Transmission

Atmospheric components absorb or scatter IR with different ratios depending on the physical properties of the atmospheric component and the wavelength of the IR. In order to accomplish thermal imaging for long distances, the atmosphere must transmit radiation with low attenuation. Scattering can be categorized as Mie scattering and Rayleigh scattering. Mie scattering can be explained as particles having a size larger than the wavelength of the light scattering the radiation without any dependence on the wavelength [7]. On the other hand, Rayleigh scattering is inversely proportional to the fourth power of wavelength and the size of the particle is smaller than the wavelength of the light [7]. Various gases in the atmosphere such as H_2O, CO_2, and O_2 absorb IR at particular wavelengths. Accumulation of the effects of the absorption and scattering of the atmospheric components form the IR bands.

There are wavelength regions where transmission of IR is relatively high which are known as atmospheric windows. Photodetectors are tailored so that they are sensitive

to these wavelength regions. Among atmospheric windows, mid-wave infrared (MWIR) and long-wave infrared (LWIR) have high transmission rates at wavelengths radiated by near room temperature objects. These windows are suitable choices for infrared thermal imaging applications. Figure 1.2 shows the transmittance of radiation in atmosphere up to 14 µm and Table 1.2 shows the subregions of the infrared radiation.

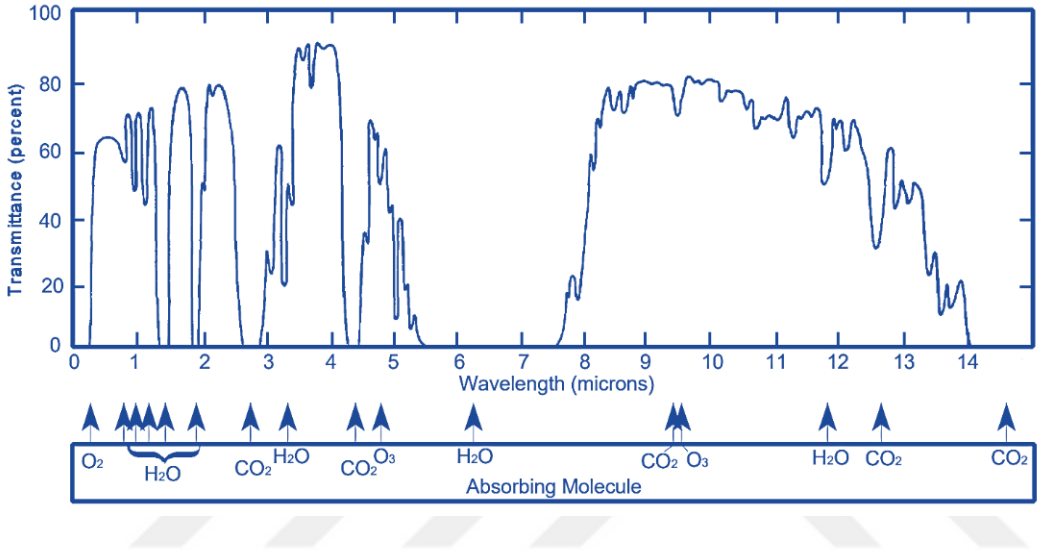

Figure 1.2 Transmittance of atmosphere in the infrared region over 1 nautical mile at sea level [8]

Table 1.2 Subregions of the infrared region and corresponding wavelengths

Infrared Region	Wavelengths
Near Infrared (NIR)	0.7 µm - 1.0 µm
Short-wave Infrared (SWIR)	1 µm – 3 µm
Mid-wave Infrared (MWIR)	3 µm – 5 µm
Long-wave Infrared (LWIR)	8 µm – 14 µm
Very Long-wave Infrared (VLWIR)	14 µm – 30 µm
Far Infrared (FIR)	30 µm -100 µm

1.2 Main Infrared Photodetector Types for Thermal Imaging

With the application of various material compositions and technical aspects, IR detectors can be fabricated in regions from NIR to VLWIR. IR emitted by objects can change the total current flowing through the semiconductors. This change due to IR can be sensed, and information can be obtained about the object. The change in current can occur optically or thermally. Incident photons can cause band transitions and result in current flow through the semiconductor. Under constant bias voltage, optical power is measured by sensing the flowing current. These types of detectors are referred to as photon detectors. They have very short response time and high responsivity [9, 10]. If the application requires high sensitivity and high frame rates, a photon detector may be the proper choice. However, performance comes with drawbacks. Fabrication costs of photon detectors are relatively high, and they may require cooling systems to reduce the undesired current flow created by thermally generated carriers. On the other hand, an incident photon can cause heat on the semiconductor and results in temperature change. By sensing the resistance change due to temperature change caused by the photon incidence, optical power can be measured. These types of detectors are referred to as thermal detectors. They have slower response times, lower responsivity, and can operate near room temperatures [9, 10]. Thermal detectors may be the cost-effective solution unless high performance is desired. Generally, the choice between photon detectors and thermal detectors depends on the requirements of the application.

Photoconductors are basic photosensitive materials that exhibit conductivity change when a photon is absorbed. Incident radiation promotes electrons from the valance band to the conduction band and creates free electron and hole pairs in semiconductor. These pairs are referred to as carriers and can contribute to the conductivity of the material. In order to collect the carriers generated by radiation, a bias voltage must be applied. The bias voltage requirement of the photoconductors is relatively higher due to the absence of the built-in electric field. Furthermore, there

is not any potential barrier for undesired current flow, therefore, photoconductors exhibit relatively higher dark current characteristics.

Photovoltaic detectors are electronic devices which generate electrical current with incident radiation that has sufficient energy through the photovoltaic effect. P-n junction photodetector is a type of photovoltaic detector. It is fabricated by doping the semiconductors with donors and acceptors to form the p-n junction where a very high electric field is formed in a very short region. This region is called depletion region. When a photon strikes the semiconductor materials, an electron is excited from the valence band to the conduction band by creating an electron-hole pair. The electric field sweeps these carriers to the contacts and current flow occurs. The carrier generation due to incident photon must be in the depletion region or must be in a distance of diffusion length to induce current flow. Other carriers generated in other regions cannot contribute to the current flow and recombine before reaching contacts. The existence of the built-in electric field eliminates the requirement of the external bias voltage, and the potential barrier reduces the undesired majority carrier flow. InSb, InGaAs, and HgCdTe are the bulk materials which are used to fabricate photovoltaic photodetectors for IR.

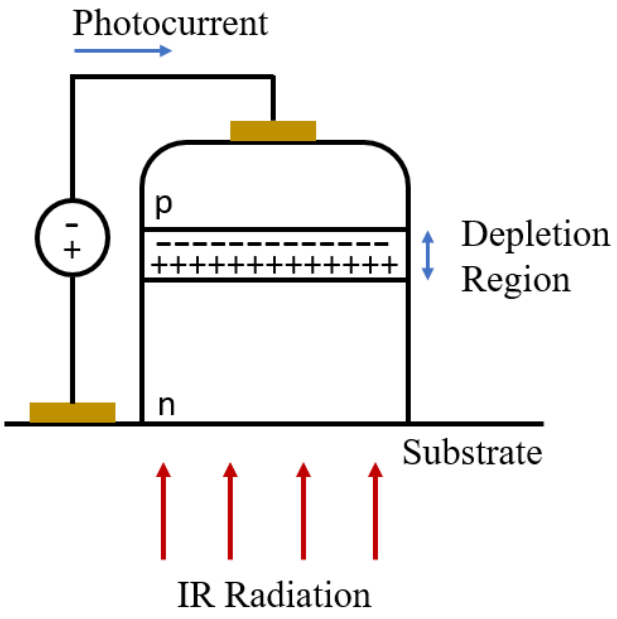

Figure 1.3 An illustration of a photovoltaic detector

Quantum well infrared photodetectors (QWIPs) are a type of photoconductor that is bandgap engineered so that bulk semiconductors that is not able to sense the IR due to a relatively large bandgap can detect the IR. In QWIPs, small bandgap materials are sandwiched between large bandgap materials to form quantum wells. Quantized states in quantum wells are tailored so that the energy difference between states is close to the energy of the photon which is intended to be absorbed. There are various approaches for calculating the energy levels of the quantum wells and they can be used to optimize detector structure [11, 12, 13]. QWIPs are typically fabricated with III-V materials such as GaAs/AlGaAs and InP/InGaAs. Mature fabrication techniques of these material systems enable easy and repeatable production, high uniformity and fewer defects. On the other hand, the main bottleneck of QWIPs is the inability of absorption of normal incident radiation resulting in lower quantum efficiency (QE) values. Optical couplers can be utilized to increase the QE [14]. Besides, some examples (also photodetectors in this thesis work) can detect portion of normal incident radiation [15, 16]. Moreover, photocurrent in QWIPs is generated through majority carriers. Therefore, QWIPs have relatively higher dark current levels and require lower operating temperatures

[17]. Figure 1.4 illustrates a band diagram of QWIP where excitation and tunneling to the continuum band are shown.

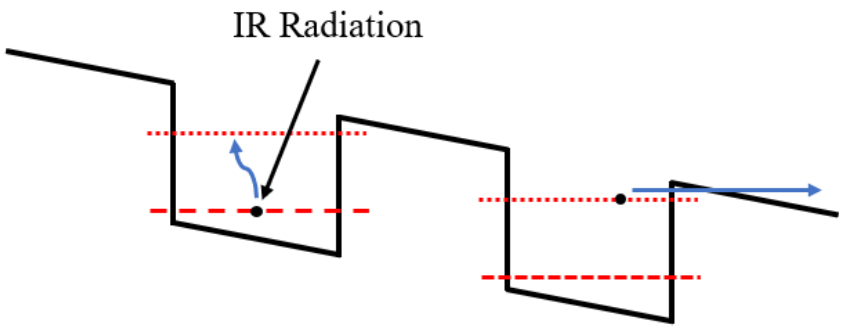

Figure 1.4 An example of the conduction band diagram of QWIP

Type II superlattice detectors (T2SLs) are also quantum-structured devices. Quantum wells in QWIPs are separated with thick barriers and the electrons in different well regions do not interact with each other. In T2SL photodetectors, thin layers with extended electron wavefunctions are fabricated with type II misalignment to create artificial bandgap. The interaction of thin layers can be identified by the overlapping of the wavefunctions which creates the minibands. These minibands can be tailored by changing the materials or thicknesses of the layers. The energy difference between minibands specifies the absorption wavelength. InAs/GaSb layers on a GaSb wafer can be exemplified as a T2SL device structure. One of the challenges of the T2SL is the complication of the growth process since the material composition and thickness of the layers must be precisely controlled to form the desired structure [18].

Microbolometers are a type of thermal detector offering inexpensive solutions for IR detection without any requirement of cryogenic cooling. They sense the temperature change caused by thermal radiation. A thin film whose electrical resistance is sensitive to its temperature is suspended as an absorbing layer and that resistance change is sensed by the readout circuitry. The thin film is generally made of vanadium oxide [19]. Microbolometers are not as sensitive as photon detectors and cannot provide low response time due to the heat capacitance of the physical

structures. On the other hand, they are cost-effective solutions to photon detectors for thermal imaging.

1.3 Infrared Photodetector Figures of Merit

In order to evaluate the performance of the photodetectors and focal plane arrays, figures of merit are introduced in this section.

1.3.1 Responsivity

Responsivity is the measure of how well a photodetector generates an electrical signal in response to incident optical power. Amperes per watt (A/W) or volts per watt (V/W) are expressed as the unit of the responsivity, depending on whether the photodetector generates current or voltage as an electrical signal. Responsivity of a detector which generates photocurrent in response to optical power can be written as [20]

$$R(\lambda) = \frac{Output\ Signal}{Incidet\ Power} = \frac{I_{photo}}{\phi_e A} \tag{1.9}$$

where ϕ_e is the incident optical power per unit area and A is the active area of the photodetector. Photodetectors' responsivity generally varies with the wavelength of the incident radiation. Therefore, responsivity is expressed as a function of wavelength. The photocurrent of the detector depends on the gain (g), quantum efficiency (η), and total incident optical power. Quantum efficiency is the measure of how effectively a photodetector absorbs a photon and gain is the number of generated electrons contributing to photocurrent due to an absorbed photon. The total photocurrent can be represented as [20]

$$I_{photo} = q\eta g\phi_p A \tag{1.10}$$

where q is the elementary charge, ϕ_p is the number of photons incident on the detector per unit time per unit area. The relationship between ϕ_p and ϕ_e is:

$$\frac{\phi_e}{hc/\lambda} = \phi_p \qquad (1.11).$$

By using equations (1.9), (1.10), and (1.11) spectral responsivity can be also written as

$$R(\lambda) = \eta g \frac{q\lambda}{hc}\ A/W \qquad (1.12).$$

1.3.2 Dark Current

The dark current of a photodetector is the undesired current flow even in the absence of incident radiation. The amount of the dark current is affected by the photodetector technology, material composition and quality, and operating temperature. Usually, the main reason for the dark current is the thermally generated carriers inside the semiconductor material. Photodetectors can be cooled down to reduce the amount of dark currents. The optimum operating temperature of the photodetectors and their performance can be limited by the dark current. The dark current can increase the noise level of the signal and can be an issue in low-light-level applications.

1.3.3 Noise

The noise level of a photodetector is a critical parameter. In this section, Johnson, generation-recombination, shot and *1/f* noises are briefly discussed.

Johnson (thermal) noise, also known as thermal noise, arises from the random motion of carriers in a conducting material due to their thermal energy. The total Johnson noise increases with increasing temperature. It does not show any frequency-related characteristics (white noise). Johnson noise current given as:

$$i_{n,Johnson} = \sqrt{\frac{4k_b T\Delta f}{R}} \tag{1.13}$$

where k_b is the Boltzmann constant, T is the temperature, R is the dynamic resistance of the photodetector, and Δf is the measurement bandwidth.

Generation-recombination (G-R) noise arises from random generation and recombination of the charge carries inside the semiconductor material. Generation and recombination processes can be generated thermally or optically. The total G-R noise is given by

$$i_{n,G-R} = \sqrt{4qIg\Delta f} \tag{1.14}$$

where I is the total current of the photodetector, q is the elementary charge, g is the device gain and Δf is the measurement bandwidth.

The total current of a photodetector is the summation of dark current and photocurrent. Then noise equation for G-R noise becomes

$$i_{n,G-R} = \sqrt{4q(I_{photo} + I_{dark})g\Delta f} \tag{1.15}.$$

If the radiation incident on the detector is sufficiently high, the photocurrent becomes much larger than the dark current and the detector shows background limited performance (BLIP). Then, the G-R noise equation reduces to

$$i_{n,G-R} = \sqrt{4qI_{photo}g\Delta f} \tag{1.16}.$$

For photovoltaic detectors, recombination processes are not random, and the gain of the detector is unity. This type of noise is known as **shot noise**. Shot noise of a photovoltaic detector under BLIP condition is given as [21]

$$i_{n,Shot} = \sqrt{2qI_{photo}\Delta f} \quad (1.17).$$

***1/f* noise (pink noise)** is also observed in many electronic systems. It degrades the performance of the photodetector especially at low frequencies. As the name implies, the characteristic of *1/f* noise decreases with increasing frequency. The origin of *1/f* noise is not known but imperfections and trap states inside the photodetector material can create this noise.

There are various noise sources in photodetectors and their total effect can be computed as

$$i_{n,total} = \sqrt{{i_{n,Johnson}}^2 + {i_{n,G-R}}^2 + {i_{n,1/f}}^2 + {i_{n,Shot}}^2} \quad (1.18).$$

1.3.4 Detectivity

Responsivity can represent how well a photodetector is sensitive to IR. However, it does not represent the actual performance of a photodetector since responsivity does not consider the total noise in the device. Therefore, a parameter that considers both responsivity and noise performance should be defined. Detectivity is a term defined as the reciprocal of the noise equivalent power (NEP). NEP signifies the optical power level required to produce an electrical signal equal to the noise level of the photodetector. The detectivity can be computed as

$$D = \frac{1}{NEP} = \frac{R_i}{i_{n,total}} \quad (1.19)$$

where D is the detectivity $i_{n,\text{total}}$ is the total noise of the photodetector and R_i is the current responsivity of the photodetector. Moreover, detectivity may not be a proper metric while comparing two different photodetectors, because the value of detectivity changes with the area and measurement bandwidth. By normalizing the detectivity value with them, specific detectivity (D*) is calculated. D^* is expressed as

$$D^* = \frac{R_i}{i_{n,total}}\sqrt{A\Delta f} \tag{1.20}$$

1.3.5 Noise Equivalent Temperature Difference

In order to quantify the thermal imaging performance, noise equivalent temperature difference (NETD) can be specified. It is the measure of the required temperature difference to produce a signal that has equal power to the total noise power. The expression of NETD is given as [22]

$$NETD = \frac{(1 + 4f/\#^2)\sqrt{\Delta f}}{\sqrt{A}\int_0^\infty T(\lambda)D^*(\lambda)\frac{dM_{target}(\lambda)}{dT}d\lambda} \tag{1.21}$$

where *f/#* is the f-number of the optics, *Δf* is the bandwidth of the measurement, *A* is the active area of the detector, *M(λ)* is the spectral exitance of the target, *D*(λ)* is the specific detectivity, *T(λ)* is the transmission coefficient of the air. A smaller NETD value indicates better thermal sensitivity. Smaller f-number and longer integration times can be used to obtain low NETD values. Therefore, while stating a NETD value, f-number and integration time should also be specified.

1.4 Objective of The Thesis Work

This thesis study focuses on the demonstration and characterization of two 640x512 format and 15 μm pitch QWIP FPAs operating in the MWIR band. The characterized QWIP FPAs in this study are based on strained InP/$In_{0.85}Ga_{0.15}As$ and InP/InAs material systems. Utilization of these material systems enables detection of normal incident radiation. Therefore, FPAs yields desirable performances without diffraction gratings. Both FPAs can perform NETD value of as low as 20 mK enabling high performance thermal imaging. Although both FPAs have strained epilayer structure, FPAs yield high uniformity and correctable performance without

having any stability problem. All of these features can be offered even with very low pitch values.

Chapter one presented the basics of IR detector technology. Chapter two gives theoretical information about the characteristics and operation principle of QWIPs and covers the literature survey including light coupler schemes, available material systems for the fabrication of QWIPs and QWIP based FPA examples on GaAs and InP substrates. In chapter three, details of the InP material system are discussed and FPA characteristics of InP/$In_{0.85}Ga_{0.15}As$ and InP/InAs based QWIP FPAs are presented with NETD performance comparison with the literature. Finally, chapter four concludes the thesis work and includes future work.

CHAPTER 2

QUANTUM WELL INFRARED PHOTODETECTORS

QWIP technology allows sensing of infrared radiation with large bandgap semiconductor materials making the production easier and more repeatable. Moreover, detection wavelengths can be tailored for different infrared regions. With these features, QWIP is one of the significant infrared sensing technologies. The first QWIP was developed in 1987 being sensible in the LWIR band [4], and it is followed by the first QWIP FPAs in 1991 [23, 24]. This chapter introduces and summarizes the fundamentals, different material systems, fabrication, and examples of QWIPs.

2.1 Operation and Characteristics of QWIPs

Apart from low bandgap material-based IR detectors which involve interband transitions, QWIPs involve intersubband transitions. The intersubband transitions occur in a quantum well region. Large and small bandgap semiconductors are used to form the barriers and wells. In the well region, the energy levels are quantized, and electrons can only occupy quantized energy levels. Moreover, by gathering multiple quantum wells (MQWs), the absorption region can be extended. However, each well must be independent quantum mechanically from each other to prevent the electron tunneling between quantum wells. This is ensured by utilizing thick barriers. A period of QWIPs is illustrated in Figure 2.1 showing an electron transition from ground state to first excited state due to IR radiation absorption and regions of the high bandgap and low bandgap materials.

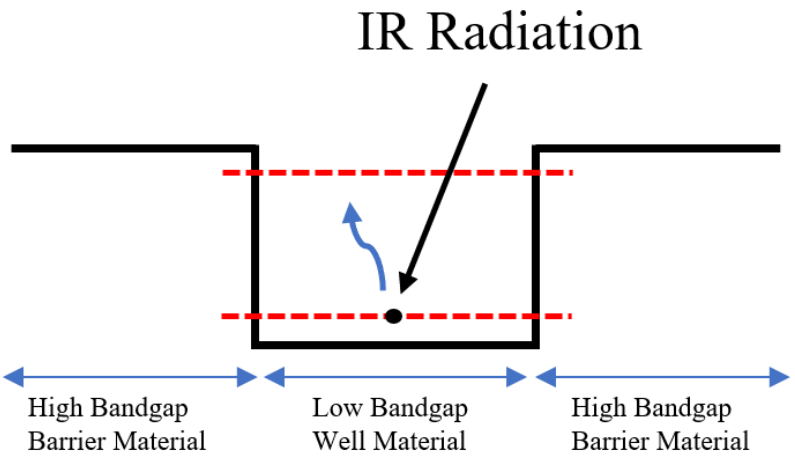

Figure 2.1 A period of quantum well band diagram

The absorption of IR in QWIPs promotes an electron from the quantized ground state to the quantized first excited state or continuum band. Consequently, excited electrons can be swept to collector contact under a potential difference and contribute to the total current passing through the device. Excited electrons can also be captured by other wells with capture probability of p_c while flowing through the device without any contribution to the total current. Figure 2.2 shows the operation principle of a QWIP.

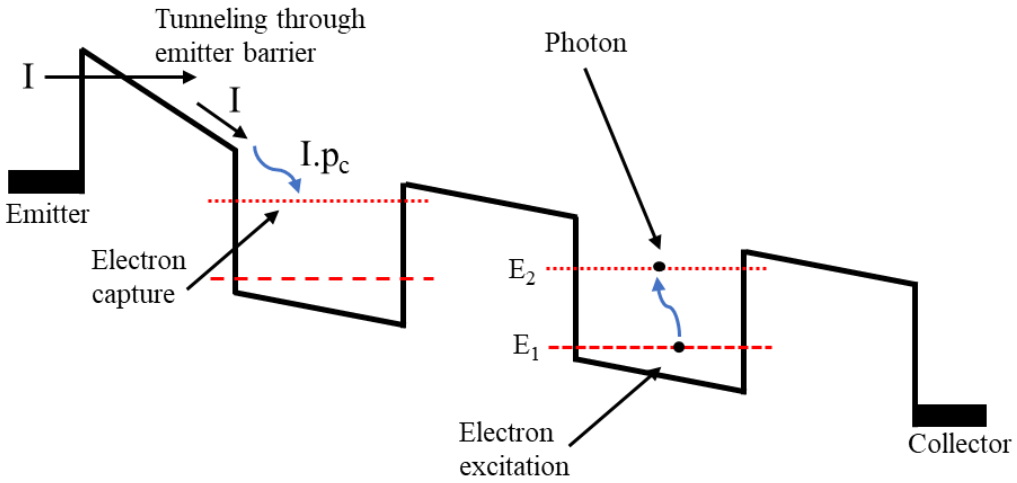

Figure 2.2 Operation principle of QWIP (redrawn after [25])

The peak wavelength of the QWIP can be tailored by adjusting the energy difference between the quantized ground state and the quantized first excited state. The level of these energy states depends on the well width and barrier height of the QWIP. The well width can be adjusted by the dimension of the well material and the barrier height can be adjusted by the compositions of the well and barrier materials. Furthermore, by solving the Schrödinger equation, the peak absorption wavelength can be estimated.

QWIPs can be classified according to the energy level of the first excited state. In bound-to-bound (B-B) QWIPs, the first excited state is below the top of the potential barrier distinctly, and the promoted electrons from the quantized ground state must tunnel through a small portion of the potential barrier. This can be accomplished by applying high voltage bias which bends the energy band diagram and thinners the potential barrier. This type of QWIP has the highest peak QE thanks to high wavefunction coupling between quantized states. On the other hand, in bound-to-continuum (B-C) QWIPs, electrons directly promote from the quantized ground state to the continuum band which is above the potential energy of the barrier. In the continuum band, there are various energy states separated by very low potential energy. Therefore, B-C QWIPs have a broader responsivity spectrum. B-C QWIP does not require high bias voltage since promoted electrons must not tunnel through any potential barrier. However, the thermally promoted electrons result in larger dark currents than that of B-B QWIP. The last type is bound-to-quasibound (B-QB), in which the quantized first excited states are barely below the top of the potential barrier. B-QB QWIP shows characteristics between B-B QWIP and B-C QWIP. Figure 2.3 illustrates the energy band diagram of all three types of QWIP.

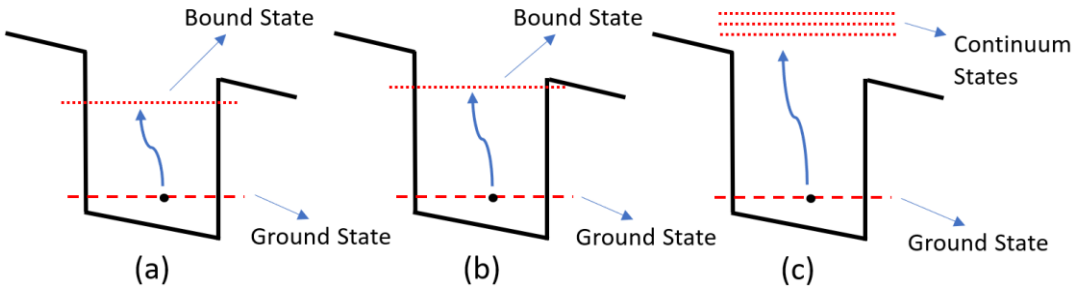

Figure 2.3 (a) B-B QWIP band diagram (b) B-QB QWIP band diagram (c) B-C QWIP band diagram

2.1.1 Intersubband Transitions

The total transition rate due to the absorption of photons between the quantized ground state and the excited state can be described by Fermi's Golden rule [26]

$$W = \frac{2\pi}{\hbar}\sum_{f,i}|M|^2 F_i(1-F_f)\delta(E_f - E_i - \hbar w) \tag{2.1}$$

where F_i and F_f are the fermi factors of the initial and final states of the transition, $\hbar w$ is the energy of the photon, and M is the matrix element given as [26]

$$M = \frac{q}{m^*}\sqrt{\left(\frac{\phi h}{2\varepsilon_0 n_r m^* c}\right)}\left(\delta_{k_{x,y}}\delta_{k'_{x,y}}\right)\sin\theta\,\langle\psi_{z,n'}|p_z|\psi_{z,n}\rangle \tag{2.2}$$

where m^* is the effective mass of the electron, θ is the incidence angle of the photon, and n_r is the refractive index of the material. Under the assumptions of zero temperature and weak excitation, equation (2.2) can be evaluated and the QE of QWIP is defined as [26]

$$\eta = \frac{q^2 h}{4\epsilon_0 n_r m^* c}\frac{\sin^2\theta}{\cos\theta}n_{2D} f\delta(E_f - E_i - \hbar w) \tag{2.3}$$

where n_{2D} is the two-dimensional electron density in the well region, w is the angular frequency of the incident photon, and f is the oscillator strength defined as [27]

$$f = \frac{2mw}{\hbar}|\langle\psi_2|z|\psi_1\rangle|^2 \quad (2.4).$$

In equation (2.3), the absorption QE is dependent on the incidence angle of the photon, and the probability of absorption of a photon is zero for $\theta = 0^o$. Therefore, QWIPs do not respond to normal incident radiation. This phenomenon is attributed to the polarization selection rule. On the other hand, the band mixing effect may be the cause of the breakdown of the polarization selection rule which is not rigorous for all designs [26]. There are examples of having responses to normal incident radiation [15, 16].

2.1.2 Dark Current Characteristics

The total dark current of a photodetector is a crucial parameter for the detection of low-level radiation. The dark current of the QWIPs should be low enough to have a reasonable operating temperature and to obtain a high signal-to-noise ratio (SNR) at the output. Moreover, dark current fills the charge well of the ROIC unintentionally in imaging applications. The dark current of a QWIP arises from three different mechanisms. These are direct tunneling (DI) between ground states at adjacent wells, thermally assisted tunneling (TAT) where thermally excited electron tunnels through the potential barrier of QWIP, and thermionic emission (TE) where thermally excited carriers promote to continuum band and directly contribute to current [28]. Figure 2.4 shows all three-dark current mechanisms.

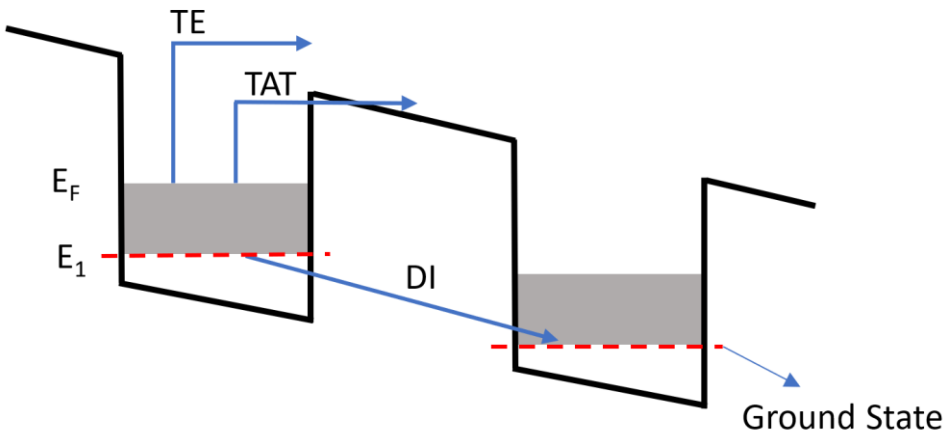

Figure 2.4 Dark current components of a QWIP

Among these dark current components, thermionic emission-based dark current is the dominant dark current source at 70 K and higher temperatures in QWIPs having a 10 μm cutoff wavelength [29]. Since the transport mechanism of TE current is similar to photocurrent, suppressing this component may not favor the photocurrent to the dark current ratio in some cases [29]. At temperatures between 45 K and 70 K, the total dark current is dominated by the TAT current in AlGaAs/GaAs QWIP with 10 μm cutoff wavelength [29]. This type of current can be minimized with the utilization of high-quality barriers. Aluminum-free binary barriers such as InP can be preferred [30]. For very low-temperature values (<45 K), the major dark current component of QWIPs is the DI current. The dark current of the QWIPs due to TE can be given as [31]

$$I_{dark} = \frac{q^2 m^*}{\pi \hbar^2} \frac{A v_D}{L_w} \Delta_1 \exp[-(E_b - e\Delta_2 - E_f - E_1)/kT] \qquad (2.5)$$

where L_w is the well width, A is the area of the photodetector, v_d is the electron drift velocity, Δ_1 is the potential energy drop on one barrier, Δ_2 is the potential energy drop on one well, E_b is the potential barrier height E_f is the fermi energy and E_1 is the energy level of the ground state. Assuming complete ionization, the two-dimensional doping concentration is equal to the electron density of the well, therefore, fermi energy level can be calculated from the equation given below [26]

$$n_{2D} = \frac{m^* kT}{\pi \hbar^2} ln\left(1 + e^{\frac{E_F}{kT}}\right) \tag{2.6}$$

where n_{2D} is the two-dimensional electron density in the well. Since the doping concentration changes the fermi level linearly and the fermi level changes the total current exponentially, the total dark current depends on the doping density with exponential relation.

2.1.3 Photocurrent Characteristics

The relationship between the photocurrent of the QWIPs and optical power can be represented by responsivity. The current responsivity of a QWIP can be expressed as [32]

$$R = \frac{q}{hv} g_p \eta \tag{2.7}$$

where g_p is the photoconductive gain, η is the total QE. The photoconductive gain can be given as [33]

$$g_p = \frac{v_d \tau_L}{l} = \frac{\tau_L}{\tau_T} = \frac{L}{l} \tag{2.8}$$

τ_L is the lifetime of the excited electrons, τ_T is the total transit time of the electrons in the device, l is the total device length and L is the average drift distance of the electrons. The photoconductive gain can be adjusted by controlling the detector bias which enhances the drift distance of the electrons. Therefore, the responsivity of the QWIPs can be increased. On the other hand, the responsivity increase is not continuous since the photoconductive gain of QWIPs saturates at high bias voltages. Figure 2.5 shows the tendency of saturation of gain and responsivity values for higher voltages.

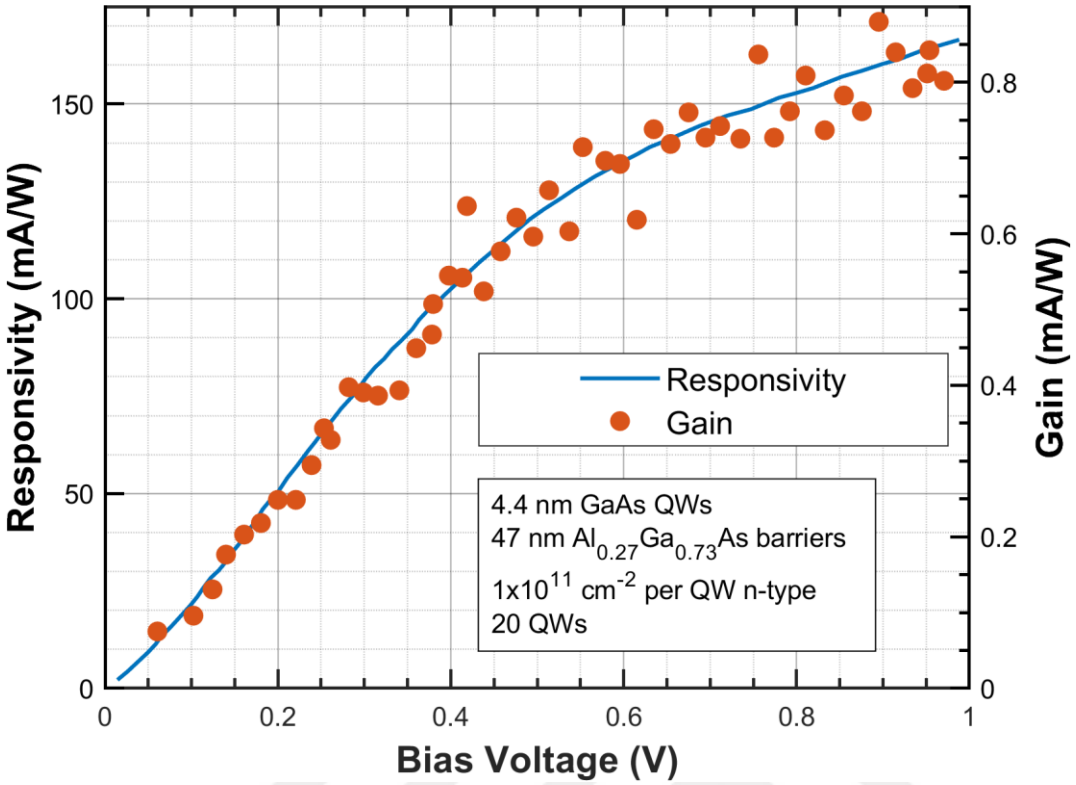

Figure 2.5 Responsivity and gain characteristics of a standard AlGaAs/GaAs of a QWIP for different bias voltages (redrawn after [34])

2.1.4 Noise and Detectivity

The QWIPs are generally free of *1/f* noise and the thermal noise is negligibly small. Therefore, the dominant noise mechanism of the QWIPs is the G-R noise resulting from random fluctuations in the number of electrons. The G-R noise of the QWIP can be given as [32]

$$I_{n,G-R} = \sqrt{4qg_n(I_{dark} + I_{photo})\Delta f} \tag{2.9}$$

where g_n is the noise gain of the device and Δf is the measurement bandwidth. Since both dark current and photocurrent are proportional to the gain, G-R noise is also proportional to the gain. Therefore, the device gain does not have any influence on the device signal-to-noise ratio.

The detectivity of the QWIP is the SNR at the output signal which is normalized with the area of the detector and measurement bandwidth. Since the major noise in the QWIPs is the GR noise, the summation of dark current and photocurrent affects the total noise. Under BLIP condition, the detectivity can be expressed as [32]

$$D^*_{BLIP} = \frac{\lambda}{2hc}\sqrt{\frac{\eta}{\phi_b}} \tag{2.10}.$$

For dark current limited performance, the detectivity can be expressed as [26]

$$D^*_{Dark} = \frac{\eta}{2hc/\lambda}\sqrt{\frac{\tau_L}{n_{thermal}L}} \tag{2.11}.$$

The impact of enhancement of QE under dark current limited performance is more significant than that under BLIP condition because detectivity is proportional to QE under dark limited performance. On the other hand, it is proportional to the square root of QE under BLIP condition.

2.2 Light Couplers

The standard QWIP is not able to detect normal incident radiation. Therefore, light couplers are used to increase the absorption of the normal incident radiation. While testing a single pixel, generally, a 45º facet light coupler is used. In this method, radiation is incident on 45º cut, polished edge of the substrate, so that, incoming radiation is refracted.

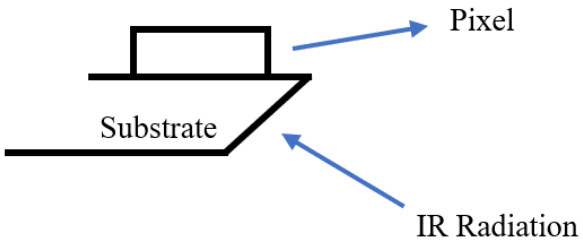

Figure 2.6 45º facet light coupler (redrawn after [35])

Typically, diffraction gratings or corrugated mesa light coupling schemes are used for FPAs. The grating structures can be fabricated on top of the pixel so that incoming radiation is diffracted and light components perpendicular to the growth direction can be created. The shape of the grating structure should be arranged according to a wavelength that is desired to be detected. In a corrugated mesa light coupler, the shape of the pixels is like a corrugated sheet. The pixels are coated with a reflecting metal layer to redirect the light into quantum wells and to create vertical light components to growth direction.

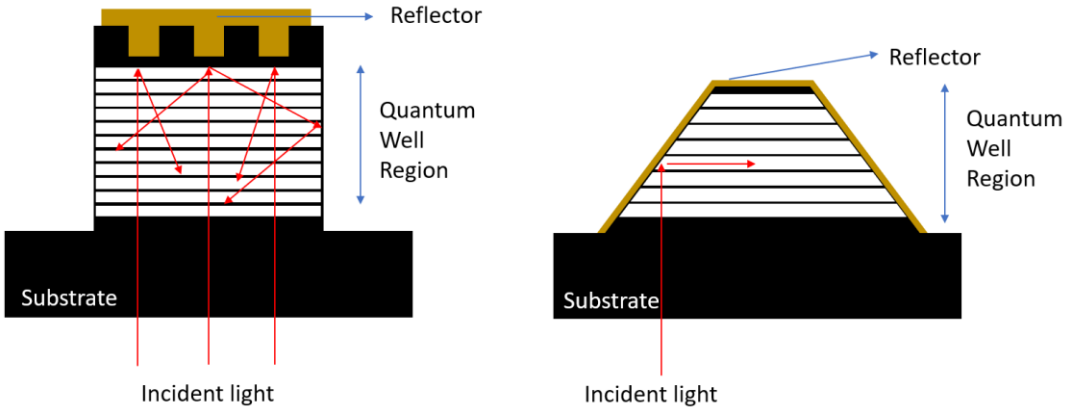

Figure 2.7 Illustration of diffraction grating (left, redrawn after [30]) and corrugated mesa (right, redrawn after [36])

2.3 Material Systems for QWIPs

In order to form the quantum wells, band discontinuity in the semiconductor device must be implemented. This can be accomplished by different types of III-V material systems. In QWIPs, III-V semiconductors are preferred due to design flexibility, maturity of fabrication processes and low cost.

2.3.1 AlGaAs/GaAs

AlGaAs/GaAs is the most mature material system in QWIPs on GaAs substrate. Owing to the lattice match between AlGaAs and GaAs for different aluminum and gallium mole fractions, photodetectors having peak response wavelengths from 4.2 μm to 26.9 μm (ranging from MWIR to far-infrared) can be fabricated [37, 38]. This material system is generally used in LWIR detection having an Aluminum mole fraction of around 0.30, also known as "Standard QWIP". However, it has limited performance for high frame rate and low background conditions due to low QE. Furthermore, AlGaAs/GaAs material system is not preferred for MWIR sensing due to the requirement of an Al mole fraction larger than 0.45 in barrier material which increases the total device dark current due to energy crossing of the Γ and X valleys decreasing the thermal activation energy of the ground state electrons [39].

2.3.2 AlGaAs/InGaAs

AlGaAs barrier and InGaAs quantum well is an alternative material system on GaAs substrate instead of AlGaAs/GaAs for MWIR sensing with higher sensitivity [39, 40]. Due to lattice match between well and barrier materials, the layer thickness of InGaAs well should be adjusted carefully. Multi-color and multi-band infrared detectors can be fabricated with the utilization of AlGaAs/GaAs and AlGaAs/InGaAs together on GaAs substrate [41].

2.3.3 AlInAs/InGaAs

Lattice-matched AlInAs/InGaAs can be used as an alternative to strained AlGaAs/InGaAs on InP substrate in the MWIR band applications. By using different quantum well widths, photodetectors having 4.15 μm and 4.9 μm cut-off wavelengths can be fabricated [42].

2.3.4 InP/InGaAs

The low quantum efficiency of the GaAs substrate-based material system overshadowed the QWIP technology and prevented it from reaching its true potential. The combination of the favorable electron transport mechanism of the InP barrier material and the low effective mass of the InGaAs well can enlighten QWIP technology again. The lattice match configuration in this material system yields photodetectors having around 8 μm peak wavelength [43]. However, the utilization of strain can extend the peak wavelength, and high performance FPAs operating in LWIR can be fabricated [44, 45]. By using InGaAsP in the well material instead of InGaAs, the peak wavelength can be also extended without causing any lattice mismatch [46]. InP/InGaAs QWIPs operating in the MWIR band can also be fabricated with the usage of high In mole fraction in well material. These types of photodetectors can sense the portion of normal incident radiation allowing the production of QWIP FPAs which do not require any light coupler [47].

2.4 Fabrication of QWIP based FPAs

In order to form the physical structure of photodetectors, thin layers are deposited on the substrate with atomic precision. This method is also called epitaxial growth. Typically, two advanced growth technologies which are Molecular Beam Epitaxy (MBE) and Metal Organic Vapor Deposition (MOCVD) are used. In this thesis study, thin layers were deposited with MBE on the InP substrate.

Fabrication of the detectors continues with several microfabrication steps. In each step, patterning is realized by the UV photolithography technique. First, the whole wafer is coated with photo-definable material called photoresist. Then, the regions to be processed are exposed to UV light to change the chemical behavior of the photoresist so that UV exposed photoresist can be removed by developers. Non-exposed regions remain photoresist coated, therefore, are not affected by the fabrication step. The first step is the forming of the alignment marks to implement fabrication steps in accordance. After that, the desired diffraction grating structure is patterned and formed with a wet/dry etching process to increase the total absorption. Then, the wet/dry mesa etching process is applied to create pixels without disturbing the ground (bottom) contact connection. Top ohmic contacts must be formed to have an electrically proper connection with pixels. This is done by evaporating contact metal and diffusion of it with annealing at high temperatures. In order to increase the absorption further, another metal layer can be deposited to reflect unabsorbed radiation. The surface states at the edges of the pixel structure may cause undesired current flow. This can be prevented by coating the wafer with passivation material without coating the top contact regions. Indium bumps must be formed on the top of the pixel to bond the pixel array to ROIC. However, under bump metallization must be evaporated before this process to protect the device from the diffusion of indium atoms. After the formation of sticky bumps, the wafer is diced into a single FPA and the FPA is flip-chip bonded to ROIC. The space between ROIC and FPA are underfilled with epoxy to strengthen the mechanical properties. Finally, the substrate of the FPA is thinned and anti-reflection material is coated to reduce the reflection of radiation from surface. The summary of the fabrication process is illustrated in Figure 2.8. The fabrication steps of the FPAs in this thesis work do not involve grating etch.

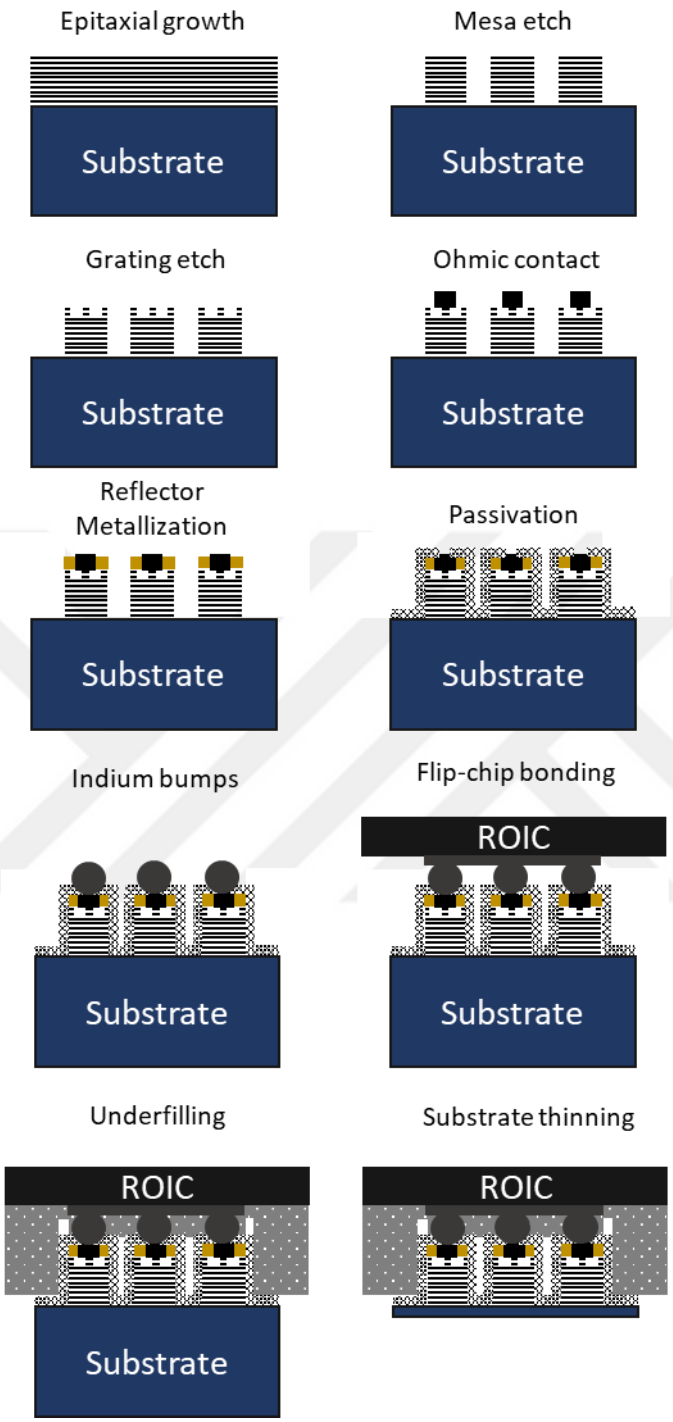

Figure 2.8 Summary of the fabrication processes of an FPA (redrawn after [30])

2.5 Examples of QWIP FPAs from the Literature

Thanks to mature fabrication processes of the QWIP technology, FPAs having high pixel operability and uniformity can be fabricated in large formats. For years, researchers have worked on GaAs-based QWIPs. However, incorrect selection of material system caused the disfavor of QWIP technology. Recent developments on InP-based QWIP FPAs can be a mind changer and enable this technology to be used more widely in thermal vision applications. In this part, GaAs-based, InP-based, and multi-band QWIP FPAs are discussed.

A large format QWIP FPA having 1024x1024 pixel size was demonstrated by Gunapala et. al. [48] in LWIR and MWIR. MWIR FPA had a two-dimensional grating structure on the top of pixels. The absorber region consisted of two coupled quantum wells to broaden the spectrum of responsivity which had a 5.1 μm cut-off [48]. The length of the well region was 40 Å where 20 Å $In_{0.3}Ga_{0.7}As$ was sandwiched between 10 Å GaAs layers [48]. The coupled wells were separated with undoped $Al_{0.3}Ga_{0.7}As$ having a length of 40 Å. The length of the barrier region between uncoupled quantum wells was 400 Å [48]. On the FPA side, the actual area of a pixel was 17.5x17.5 μm^2 and the pitch of the array was 19.5 μm. At operating conditions of 1 V reverse bias, 95 K temperature with f/2.5 optics and 60 ms integration time, the FPA yielded 17 mK mean NETD [48]. The NETD non-uniformity of uncorrected data was 5.5% [48]. On the LWIR side of the study, photodetectors also had a grating structure, and the actual pixel and FPA pitch were the same as MWIR FPA [48]. The Absorber region consisted of 40 Å $Al_{0.27}Ga_{0.73}As$ quantum well width and 600 Å barrier resulting in a 9 μm cut-off wavelength [48]. With the same optics, LWIR FPA yielded 13 mK NETD at 70 K operating temperature with 29 ms integration time [48].

QWIP FPAs are also being used in space applications thanks to properties like effortless and reproducible fabrication even in large formats, low-cost, absence of *1/f* noise, and radiation hardness. Jhabvala et. al. [49] demonstrated a dual-channel imaging system where wavelength spectrum of FPAs were centered at 10.8 μm and

12.0 μm. The array had a 640x512 format with a 25 μm pitch and was operated at 43 K [49]. The f-number of the system was f/1.64 [49]. Under these conditions, the system exhibited NETD less than 33 mK at 5.5 ms integration time for both channels [49].

GaAs QWIP technology based LWIR cameras are also available commercially. Thales manufactures two kinds of cameras based on QWIP. Catherine XP offers a 384x288 image format with a 25 μm pitch and Catherine MP offers a 640x512 image format with a 20 μm pitch. Systems offer NETD value of 55 mK for integration times in the range of 3 to 5 ms. The Catherine XP camera with 4° and 3° field of view (FOV) is shown in Figure 2.9 [50].

Figure 2.9 Catherine XP in 4° FOV version on left and 3° FOV version on right [50]

In addition to standard AlGaAs/GaAs QWIPs, InP/InGaAs QWIPs show promising performance. The standard QWIP is considered as an improper choice for high-speed applications due to large integration times, however, the higher responsivity of InP-based QWIPs allows the operation at high frame rates. Higher responsivity due to the larger gain of this material system was reported by several groups [51, 52].

The first lattice-matched InP 256x256 FPA for LWIR was reported by Jiang et. al. [53]. They achieved 29 mK NETD with f/2 optics at an operating temperature of 70

K [53]. The pixel size and pitch were 25x25 μm^2 and 30 μm, respectively [53]. Ozer et. al. [54] demonstrated the first 640x512 large format InP/InGaAs QWIP FPA which yielded 40 mK NETD at 77 K with f/1.5 optics where pixel size was 21 μm. The lattice-matched mole configuration in this material system has a cut-off wavelength of around 8.5 μm which barely falls into the IR atmospheric transmission and degrades the efficiency of the imaging for long-range applications. Without perturbating the lattice match, by adding phosphorus (P) into the well region, the cut-off wavelength can be extended up to 9 μm. The first 640x512 format QWIP FPA with InP/InGaAsP material system was reported by Ozer et. al. [55]. The uncorrected DC signal nonuniformity of the array was 4.5% resulting in low spatial noise [55]. The InP/InGaAsP FPA exhibted high enough SNR performance even with submillisecond integration times, for 440 μs integration time, the reported NETD was 46 mK at 66 K operating temperature with f/1.5 optics [55].

The sensitivity wavelength of InP/InGaAs QWIPs could also be changed with the utilization of strained quantum well material. The strain could be introduced by changing In mole to control conduction band discontinuity and extend the cut-off wavelength [44]. InP/InGaAs QWIP FPA demonstrated by Eker et. al. [56] had a cut-off wavelength of 9.7 μm where In mole fraction was reduced to 0.48 from lattice-matched configuration and well width was 55 Å. With f/1.5 optics and at 65 K operating temperature, the FPA yielded NETD values of 19 mK and 40 mK at integration times of 1.8 ms and 430 μs respectively [56]. Another research on strained InP/InGaAs QWIP was conducted by Arslan et. al. [45]. The well width was 60 Å and In mole fraction was also 0.48 in this study [45]. The FPA exhibited extraordinary performance, achieving a peak quantum efficiency of 31%, enabling operation in the LWIR band with a 9 μm cut-off wavelength [45]. The NETD was below 50 mK with f/2 optics for 78 K operating temperature [45]. For 67 K operating temperature, the NETD was 30 mK with 1 ms integration time with the same optics [45].

InP/InGaAs material system could also offer QWIPs operating in the MWIR band. By using a high In mole fraction, the sensitivity wavelength could be shifted down

to MWIR [46]. A 640x512 FPA with 15 μm pitch where the epilayer structure of the device consisted of 35 Å thick $In_{0.85}Ga_{0.15}As$ well and 550 Å InP barrier was reported by Besikci et. al. [57]. This configuration was also able to detect normal incident radiation, unlike standard QWIP [57]. Thanks to that, QE could reach a value of 22% even without any light coupler [57]. A very high, 70%, peak conversion efficiency (CE) (product of quantum efficiency and gain) was also obtained [57]. The FPA yielded below 20 mK NETD with f/2 optics at an operating temperature of 78 K [57].

Multi-color and multi-band IR photodetectors are of quite an interest because they offer significant advantages such as improved target discrimination and increased temperature measurement accuracy. QWIP technology shines out with mature fabrication processes and configurable detection wavelength making it suitable for multi-color/band detectors. Typically, three different approaches can be followed to fabricate multi-color/band FPAs. In the three-contact approach, indium bumps are formed on the top of each pixel for top, mid, and bottom contacts. Another approach is the fabrication of spatially separated pixels in the FPA. However, degradation in the resolution is the main drawback. The last approach is voltage tuning in which the detection band is determined by the voltage bias across the device.

The first dual-band 1024x1024 QWIP megapixel FPA was demonstrated by Gunapala et. al. [58] on a GaAs substrate. The full-width at half maxima (FWHM) of the bands were extended from 4.4 to 5.1 μm and 7.8 to 8.8 μm for MWIR and LWIR bands, respectively [58]. At operating temperature of 68 K, the system yielded 27 mK NETD for MWIR and 40 mK NETD for LWIR [58]. For both bands, the operability of pixels was 90%, which is quite low for QWIP technology. The poor operability was attributed to via-metal bridge breakage in the three-contact approach [58].

Spatially distributed four-band 640x512 QWIP FPA was demonstrated by Bandara et. al. [59]. Four different 640x128 arrays were capable of detecting 4-5.5 μm, 8.5-10.0 μm, 10.0-12.0 μm and 13.0-15.5 μm wavelength regions. The operability of the array was 99.9% indicating the effectiveness of the QWIP technology. Each array

exhibited specific detectives higher than $1x10^{11}$ $cmHz^{1/2}/W$ at 45 K with f/2 optics for 300 K background temperature.

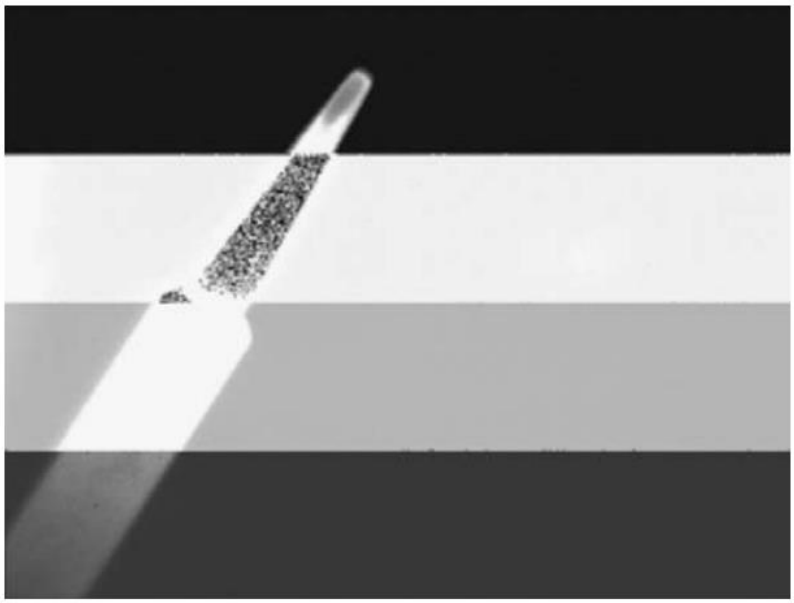

Figure 2.10 An image of soldering iron taken from spatially separated four band QWIP FPA [59]

The voltage tunable approach enables large-format FPAs and compatibility with standard single-band ROICs. Arslan et. al. [60] reported a voltage-tunable dual-band QWIP FPA operating in the MWIR and LWIR bands. The MWIR and LWIR quantum well stacks were formed with AlGaAs/InGaAs and AlGaAs/GaAs material systems, respectively. MWIR stack exhibited 14 mK NETD with an integration time of 20 ms and the LWIR stack exhibited 31 mK NETD with 3.5 ms integration time. The operability of the FPA was 99.5% for both bands showing the promise of this approach.

In this chapter, background information about QWIP technology was given and FPA examples from the literature both for InP and GaAs QWIP technology was discussed. The next chapter will present the thesis work.

CHAPTER 3

CHARACTERIZATION OF InP BASED MWIR QWIP FPAs

GaAs based QWIP technology is the most studied QWIP technology thanks to maturity level of fabrication processes, low-cost of the substrate and lattice-match between the $Al_xGa_{1-x}As$ and GaAs for various Al and Ga mole fractions. However, high Al mole fraction, which degrades the performance of the detectors due to inclusion of higher defect density and reduced thermal activation energy of the ground state electrons due to energy crossing of the Γ and X valleys which makes the AlGaAs indirect bandgap, prevents detection of IR with high SNR in the MWIR band [39]. In order to provide higher sensibility in the MWIR band and overcome high Al mole fraction issue, InGaAs QW can be used instead of GaAs QW with AlGaAs barrier [39]. In addition to AlGaAs/InGaAs material system, InP technology also provides similar level of maturity as GaAs while offering higher responsivity [61]. In this chapter, advantages of InP QWIP technology and FPA level characterization of two different MWIR FPAs which are based on $InP/In_{0.85}Ga_{0.15}As$ and InP/InAs material systems are demonstrated.

3.1 InP Based QWIP Advantages Over GaAs Based QWIP

With high enough integration times, GaAs QWIP technology demonstrates admirable imaging performance. However, if the application requires high frame rate or operability under lower photon flux conditions, GaAs QWIP technology cannot meet the requirements. The main bottleneck of the GaAs QWIP technology is the low responsivity. Moreover, the need of high responsivity becomes prominent in the MWIR band due to lower photon flux in this band from near room temperature targets. InP/InGaAs QWIPs with high In mole fraction can operate in the MWIR

band and are more responsive than GaAs based MWIR QWIPs thanks to higher photoconductive gain and quantum efficiency [62].

As stated in equation (2.3), the absorption quantum efficiency of a QWIP is proportional to two-dimensional electron density and inversely proportional to effective mass of the well region. In order to make a comparison of InP and GaAs technology in terms of absorption, effective masses of well regions of InP/InAs, InP/$In_{0.85}Ga_{0.15}As$ and AlGaAs/$In_{0.2}Ga_{0.8}As$ which is the material system in work reported by Tidrow et. al. [63] are compared. As seen from Table 3.1, materials having higher In mole fraction have lower effective mass. Therefore, larger absorption is expected for higher In mole fractions.

Table 3.1 Effective masses of InAs, GaAs and InGaAs ternary alloy

Well Material	Effective Mass (m^*)
InAs [64]	0.026
GaAs [64]	0.067
$In_{0.2}Ga_{0.8}As$ [65]	0.054
$In_{0.53}Ga_{0.47}As$ [64]	0.043
$In_{0.85}Ga_{0.15}As$ [65]	0.031

Gain characteristics of a QWIP are mainly determined by the transport properties of the barrier material. The larger gain in QWIPs consisting of InP barrier instead of AlGaAs barrier can be attributed to the larger energy spacing between Γ-L valleys in the conduction band of InP [61]. The high energy spacing provides reduced capture probability of the photoexcited electron in the well region. With the reduced capture probability of electrons, electron lifetime becomes higher resulting in higher gain values [61].

In QWIPs, drift distance of the electrons increases with the increasing applied electric field. However, after a point, increase in drift distance saturates and the gain cannot be increased further. A study reported by Arslan et. al. [45] indicates that AlGaAs/GaAs QWIP saturates at electric field value of 12 kV/cm. On the other hand, saturation occurs at larger electric field in InP/InGaAs QWIPs, therefore, they offer higher gain values. Although this study compares the LWIR AlGaAs/GaAs and InP/InGaAs QWIPs, the same observation is also expected for MWIR AlGaAs/InGaAs and InP/InGaAs or InP/InAs QWIPs because of the utilization of the same barrier material. Figure 3.1 shows the measured drift distance of the InP/InGaAs and AlGaAs/GaAs QWIPs for different electric field values [45].

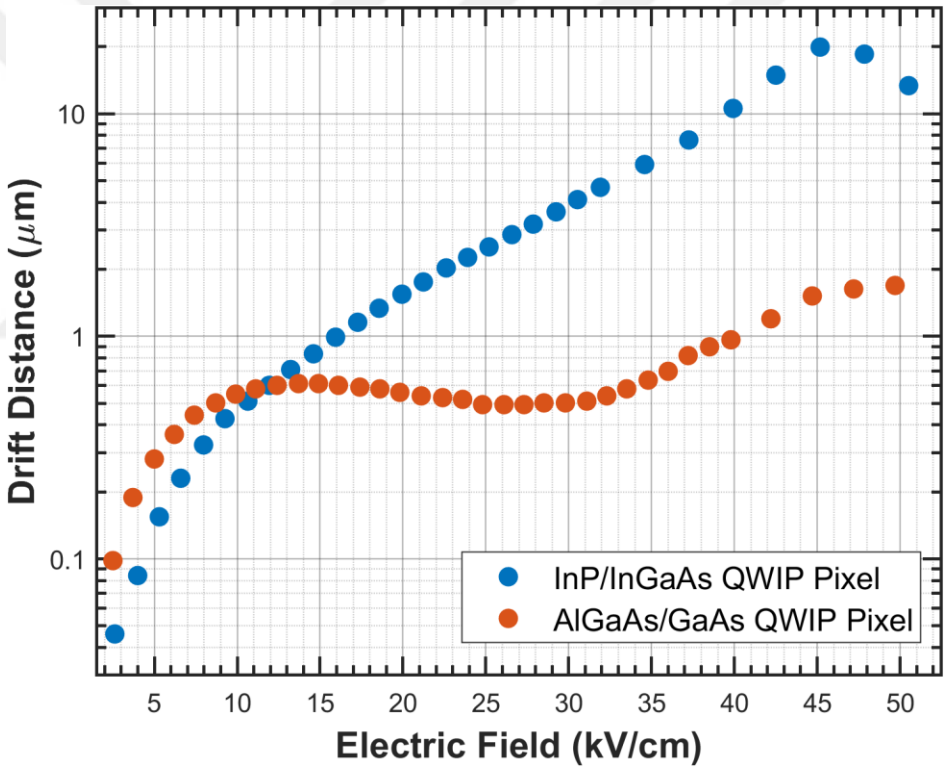

Figure 3.1 Measured drift distance of the InP/InGaAs and AlGaAs/GaAs LWIR QWIPs for different electric field values (redrawn after [45])

The photoconductive gain of a QWIP does not have any influence on SNR performance of the detector unless detector operates in charge limited conditions. When an FPA is coupled with the ROIC, the total amount of integrated charge is

limited by the electron capacity of the ROIC. Since the gain of the FPA influence the amount of integrated charge per unit time, the effect of gain on the system performance is inevitable. Under BLIP condition, the NETD of an ROIC coupled FPA can be expressed as [66]

$$NETD = \frac{k_B T^2}{hv} \sqrt{\frac{2qg}{Q_c}} \tag{3.1}$$

where Q_c is the amount of collected charge. Equation (3.1) states that for the same amount of collected charge (Q_c), the NETD of the system is proportional to the square to of the gain. In fact, low gain allows higher integration times (increases dynamic range) and the charges integrated with lower gain exhibits higher SNR. On the other hand, when the system performance is limited by the noise charge of the ROIC, the NETD of an ROIC coupled FPA is proportional to the gain of the FPA. Because the noise of the system is fixed and the signal (amount of integrated charge) linearly depends on the gain of the FPA.

There are some researches stating that QWIPs having well material of $In_xGa_{1-x}As$ with high indium mole fraction can detect portion of normal incident radiation [15, 67], therefore, they can perform higher QE even without any light coupler scheme. On the other hand, GaAs based QWIPs require light coupler in order to reach high enough QE to be used in thermal imaging applications. The elimination of light coupler also eases the fabrication of QWIPs.

GaAs QWIP technology may not meet the requirement of small pitch arrays due to need of diffraction grating. Thanks to ability of normal incident radiation sensation, high-x InP/$In_xGa_{1-x}As$ can operate with very small pitches without sacrificing absorption. Beşikci and Balci [16] reported the characteristics of very small pitch pixels based on InP/$In_{0.85}Ga_{0.15}As$ QWIP. The grating-free pixels performed characteristics excellently-scaled with the pixel area (as small as 7x7 μm^2).

3.2 Design of InP based QWIPs

The design of a QWIP depends on several factors to obtain desired detector performance in terms of sensitivity and operating conditions. The parameters that affect the total performance of a QWIP can be exemplified as barrier and well material, barrier and well width, period number and well doping level.

First of all, peak wavelength of the detection spectrum should be determined so that parameters affecting the energy levels in the well region can be assigned. The conduction band discontinuity and well width are the design parameters determining the peak wavelength. The energy discontinuity in the conduction band depends on barrier and well materials. In the case of InP/InGaAs material system, the conduction band discontinuity is determined by the In and Ga mole fractions of the InGaAs well material. Higher conduction band discontinuity results in a shorter peak wavelength. The effect of well width on the peak wavelength is not distinct as conduction band discontinuity. The increase in well width can either shorten or extend the peak wavelength. Gusakov et. al. [44] theoretically calculated the effect of well width in InP/InGaAs material system. One should also consider the well width if there is a lattice match between well and barrier material. In the case of high lattice mismatch, the growth of the epilayer may not be achievable with high enough quality.

Although barrier width does not considerably affect the peak detection wavelength, it should be wide enough to suppress the ground state tunneling between successive wells. On the other hand, excessive barrier width increases the device length unnecessarily and detector requires higher bias voltage to achieve high enough gain. Typically, barrier widths are chosen between 300 Å and 500 Å [26].

Quantum well doping level is another important parameter affecting the device performance. As stated before, absorption of incident radiation proportional to doping level in the well region. On the other hand, dark current of the device increases exponentially with increasing doping level. Therefore, to obtain the highest SNR, doping level should be optimized. Dark current level also determines the

operating temperature of the detector because high amount of dark current requires more cooling. Therefore, sacrificing photon absorption, detector operating temperature can be increased.

The period number also affects the performance of the QWIPs. It determines the gain and absorption quantum efficiency of the detector. High period number results in higher quantum efficiency due to longer absorption length, however, the ratio of electron drift distance to total device decreases which causes reduce in gain. Moreover, the number of periods in absorption region should be kept at a reasonable level so that the voltage bias across detector can establish high enough electric field in device.

3.3 Epilayer Structure and Fabrication of the InP/InGaAs and InP/InAs MWIR QWIPs

The epilayer of the QWIPs was grown with an MBE system on semi-insulating 3-inch InP substrate. The epilayer of the detectors were designed and growth of the epilayer structures were performed by Prof. Dr. C. Beşikci, InP/InGaAs FPA was fabricated by S. V. Balcı and InP/InAs FPA was fabricated by O. O. Güngör and S. V. Balcı in Quantum Devices and Nanophotonic Research Laboratory in METU respectively. The epilayer structures contain absorber region, top contact and bottom contact.

For the InP/InGaAs QWIP, top and bottom contacts were formed with $In_{0.53}Ga_{0.47}As$ layers and absorber region consisted of 30 periods of QW and barrier. One period consists of 550 Å undoped InP barrier and 35 Å doped strained $In_{0.85}Ga_{0.15}As$ quantum well. Quantum wells were n-type (Si) doped with sheet density of $5 \cdot 10^{11}$ cm^{-2}.

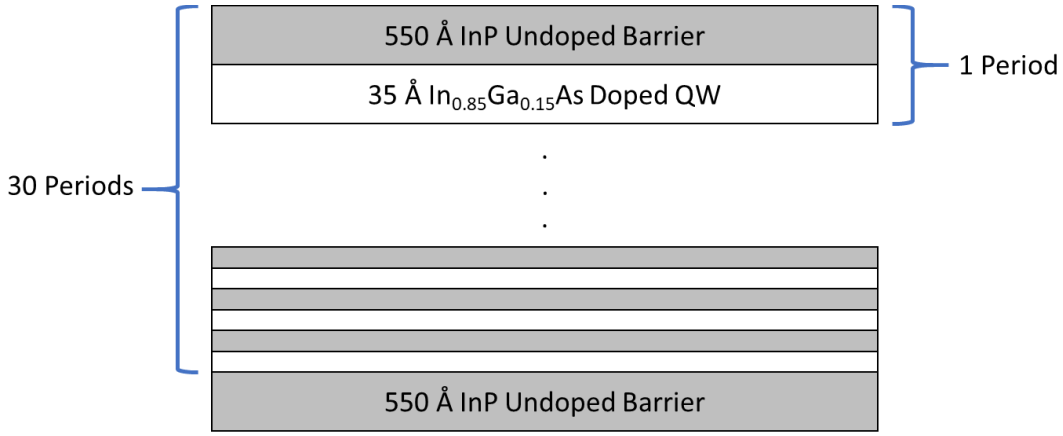

Figure 3.2 MQW structure of the InP/InGaAs MWIR QWIP

For the InP/InAs QWIP, top and bottom contacts were formed with $In_{0.53}Ga_{0.47}As$ layers and absorber region consisted 30 periods of QW and barrier. One period consisted of 550 Å undoped InP barrier and 25 Å doped strained InAs quantum well. Quantum wells were n-type (Si) doped with sheet density of $5 \cdot 10^{11}$ cm^{-2}.

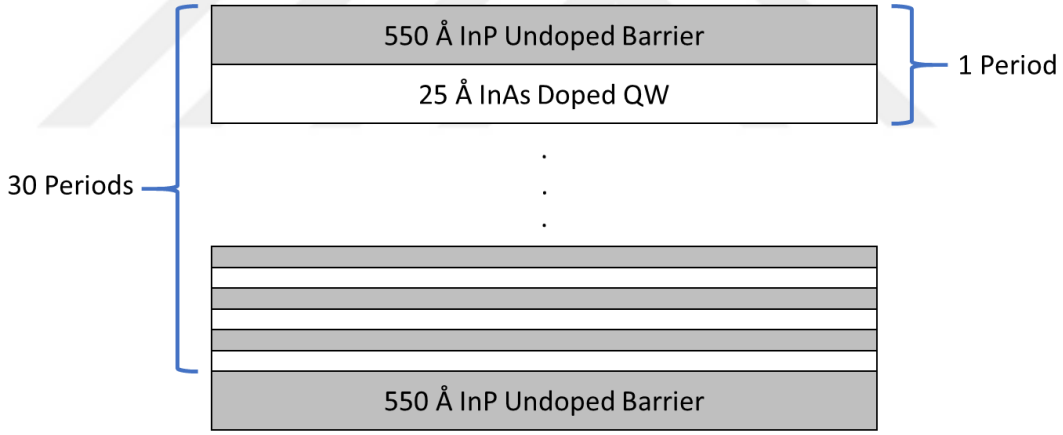

Figure 3.3 MQW structure of the InP/InAs MWIR QWIP

The fabrication steps do not include formation of diffraction grating and steps are summarized as follows:

- Formation of alignment marks with wet etching
- Formation of mesa structure down to bottom contact with wet etching
- Formation of top ohmic contact
- Passivation

- Under bump metallization
- Formation of Indium bumps
- Hybridization with a ROIC
- Substrate thinning

In this thesis work, two 640x512 pixel arrays based on the InP/InGaAs and InP/InAs material systems were hybridized with ROIC.

3.4 Pixel Characteristics of the InP/InGaAs MWIR QWIP

The pixel level characterization of the InP/InGaAs QWIP were performed by Prof. Dr. C. Beşikci and S. V. Balcı. Responsivity spectrum of the InP/InGaAs MWIR QWIP for -3.5 V bias voltage at 78 K is given in Figure 3.4. The normalized responsivity spectra of the detector were similar for different reverse bias voltages. The test pixels were not coated with anti-reflection coating. In calculations, reflection from the surface was corrected.

At -3.5 V bias, the responsivity of detector was approximately 3 A/W which is not reachable by standard GaAs based material system in the MWIR band due to low conversion efficiency. The conversion efficiency (CE) of the detector was calculated with equation (3.2) and corresponding peak CE for -3.5 V bias voltage was approximately 70%

$$R = \frac{q}{hv} CE = \frac{q}{hv} g_p \eta \qquad (3.2).$$

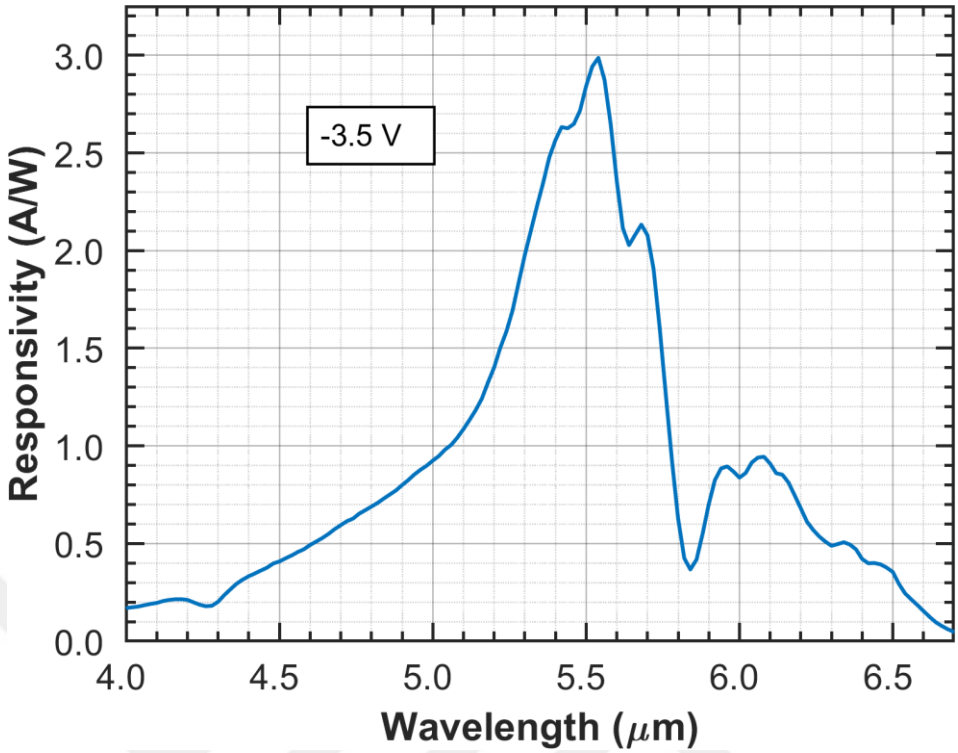

Figure 3.4 Responsivity spectrum of the InP/InGaAs MWIR QWIP at -3.5 V bias voltage at 78 K [16]

Calculated noise gain from noise measurements and photoconductive gain values are shown in Figure 3.5. The unsaturated gain in a wide bias range offers flexibility while adjusting the sensitivity of the detector according to the background flux. The noise gain of the detector starts to depart from photoconductive gain at high bias voltages. The cause of the departure of the gains can be attributed to impact ionization [68].

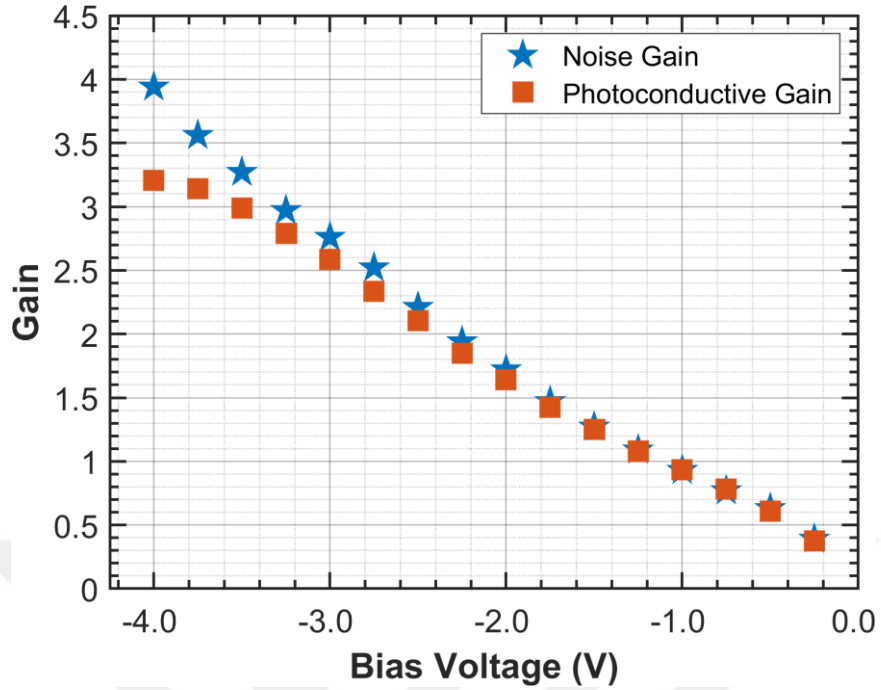

Figure 3.5 Gain of the InP/InGaAs MWIR QWIP [16]

The close relationship between noise gain and photoconductive gain in a wide range is an important factor for a QWIP FPA because the detectivity of a detector depends on the responsivity and noise characteristics. Any deviation of noise gain from the photoconductive gain causes degrade in the detectivity and so imaging performance. InP/InGaAs MWIR QWIP exhibits constant detectivity in a wide bias range enabling comparable imaging performance under different illumination conditions. The detectivity of the detectors starts to decrease beyond -3 V bias voltage, where photoconductive gain and noise gain deviates considerably. The more detailed pixel characteristics of the InP/$In_{0.85}Ga_{0.15}As$ QWIP were reported in ref. [16].

3.5 Pixel Characteristics of the InP/InAs MWIR QWIP

The pixel level characterization of the InP/InAs QWIP were performed by Prof. Dr. C. Beşikci and O. O. Güngör. Normalized responsivity spectrum of the InP/InAs MWIR QWIP for -2.0 V bias voltage at 80 K is given in Figure 3.6. The normalized responsivity spectra of the detector were similar for different reverse bias voltages.

The test pixels were not coated with anti-reflection coating and reflection from the surface was corrected. The peak responsivity for -3.5 V bias voltage was approximately 2.45 A/W and corresponding CE was 55% which is less than that of InP/InGaAs MWIR QWIP, on the other hand, InP/InAs QWIP has wider responsivity spectrum.

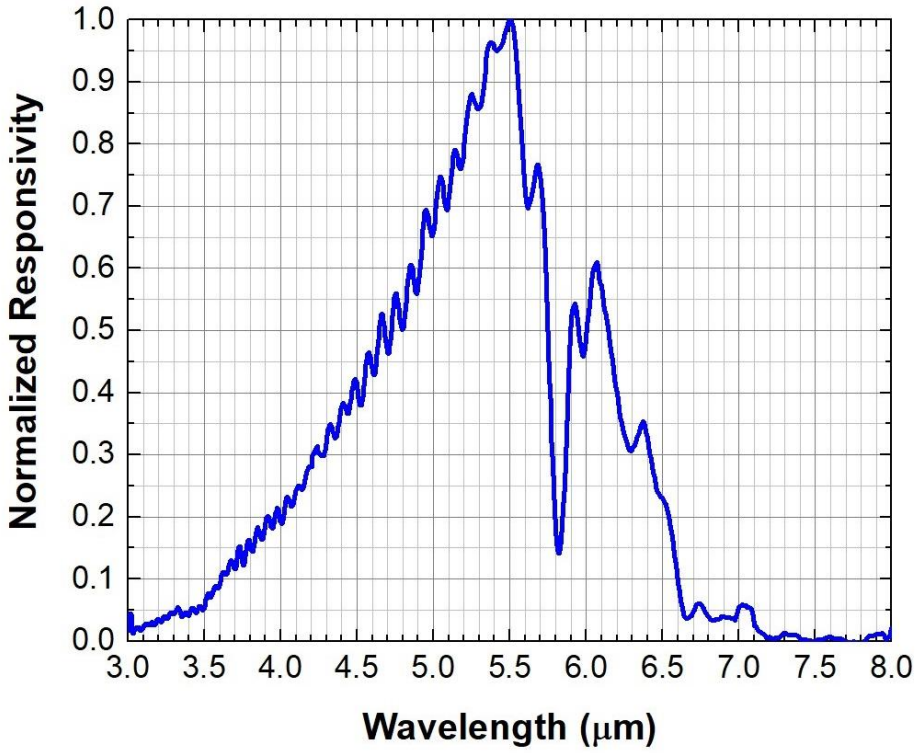

Figure 3.6 Normalized responsivity spectrum of the InP/InAs MWIR QWIP at -2.0 V bias voltage at 80 K

3.6 FPA Characterization

3.6.1 Noise Equivalent Temperature Difference

The NETD is the minimum temperature difference that can be resolved by imaging system. The calculation of NETD is as follows:

- Digital counts of sequential frames of data are recorded at blackbody temperatures of 295 K, 300 K.

- Recordings of 295 K blackbody are averaged pixel-wisely to create 295 K dataset.
- Recordings of 300 K blackbody are averaged pixel-wisely to create 300 K dataset.
- The response array is calculated by subtracting 295 K dataset from the 300 K dataset.
- Temporal standard deviation of recordings of 300 K blackbody temperature are calculated pixel-wisely to create the noise array.
- Then NETD is calculated by using equation (3.3) for each pixel where ΔT is equal to 5 K

$$NETD = \frac{array_{noise}}{array_{response}} \Delta T \quad (3.3).$$

During calculations, pixels exhibiting NETD higher than two times of the mean NETD ($2\ x\ mean_{NETD}$) were considered as inoperable pixels and those pixels were not considered in calculations. In each calculation, NETD nonuniformity was also quantified. It should be also noted that calculated nonuniformities includes the shading of the optical system. Therefore, lower nonuniformity values are expected for ideal conditions.

3.6.2 Correctability

IR FPAs are calibrated to reduce the spatial variance generated by pixels which have varying responsivities and dark current values. Usually, two-point nonuniformity (NUC) correction is applied with a linear relationship between calibration points [69]. The calibration points of the FPA was 295 K and 305 K for the calculation of correctability. A blackbody was used to form 295 K and 305 K references. Then, sequential frames were recorded to calculate the gain (G_i) and offset (O_i) coefficients of each pixel for NUC. The equations for the calculation of gain and offset values are defined as [70]

$$G_i = \frac{S_{i,295K} - S_{i,305K}}{\langle S_{295K} \rangle - \langle S_{305K} \rangle} \tag{3.4}$$

$$O_i = S_{i,295K} - G_i * \langle S_{295K} \rangle \tag{3.5}$$

where $S_{i,295K}$, $S_{i,305K}$ are the sequentially averaged signal of the i[th] pixel over 128 frames at temperatures of 295 K and 305 K respectively, and $\langle S_{295K} \rangle$, $\langle S_{305K} \rangle$ are the sample mean of sequentially averaged frames at temperatures of 295 K and 305 K respectively. After calculation of gain and offset values for each pixel, corrected pixel signal of the i[th] pixel ($S_i'(\varphi)$) from uncorrected signal ($S_i(\varphi)$), for optical power of φ, can be calculated as [70]

$$S_i'(\varphi) = \frac{S_i(\varphi) - O_i}{G_i} \tag{3.6}$$

After two-point NUC calibration, the correctability figure of merit can be calculated at specific blackbody temperature. The correctability is mathematically defined as [71]

$$c = \sqrt{\frac{\sigma_{spatial}^2}{\sigma_{temporal}^2} - 1} \tag{3.7}$$

where $\sigma_{temporal}^2$ is the average of the temporal variance of the pixels in frame, and $\sigma_{spatial}^2$ is the spatial variance which is defined as [71]

$$\sigma_{spatial}^2 = \frac{\sum_{i=1}^{n} (S_i'(\varphi) - \bar{S}(\varphi))^2}{n - 1} \tag{3.8}$$

where $\bar{S}(\varphi)$ is the spatial sample mean of the uncorrected frame, and n is the total number of the pixels.

The correctability value of 0 indicates that NUC removed the spatial variance which is created by varying characteristics of pixels. When the correctability value is 1, then, spatial variance is equal to temporal variance. For the correctability values of

higher than 1, the correction is considered as poor and fixed pattern is seen on the image degrading the imaging performance [71]. Correctability values were evaluated at 300 K blackbody temperature and NUC was applied at 295 K, 305 K blackbody temperatures. Pixels exhibiting 30% lower or larger response (from 295 K to 305 K) than mean response were not considered in the correctability calculations.

3.6.3 Random Telegraph Noise Evaluation

Although operating conditions and signal power remain unchanged, pixels exhibiting random telegraph signal (RTS) noise oscillates between at least two DC signal levels in addition to standard white noise characteristics. The correction of this kind of noise is also not possible by standard 2-point nonuniformity correction, due to uncertainty in oscillating times [70]. On the image side, as a result of RTS noise, pixels shows blinking characteristics reducing the image quality. In order to evaluate whether FPAs suffer from RTS noise, sequential frames were taken and pixels' digital counts were examined in time domain when the scene is uniform. Examination was simplified by only evaluating pixels which have high temporal standard deviation.

3.7 Characteristics of the InP/InGaAs MWIR QWIP FPA

3.7.1 NETD of the InP/InGaAs QWIP FPA

The NETD results of InP/InGaAs QWIP FPA are presented in Figure 3.7. The NETD of characterized FPA in this study was calculated at different integration times with 16-bit imager. The half-fill of the charge handling capacity of the ROIC was maintained by changing the reverse bias voltage in the measurements. Although anti-reflection (AR) coating was not applied, FPA exhibited approximately 24 mK mean NETD with f/2 optics at 13 ms integration time. Assuming that 30% percent of radiation is reflected from the surface of the FPA, up to 20% decrease in NETD is

expected when AR coating is applied. The dashed curve on Figure 3.7 is the scaled $1/\sqrt{\tau}$ fit line to emphasize that detectivity of the pixels are independent of applied reverse bias voltage because the measured NETDs follow the same trend [57]. Moreover, although the amount of integrated charge by ROIC is the same for all measurements, the NETD is smaller at higher integration times. This feature can only be offered by a sensor which offers adjustable gain. When the gain is smaller, photoelectrons are injected with less noise for unit amount of injected charge.

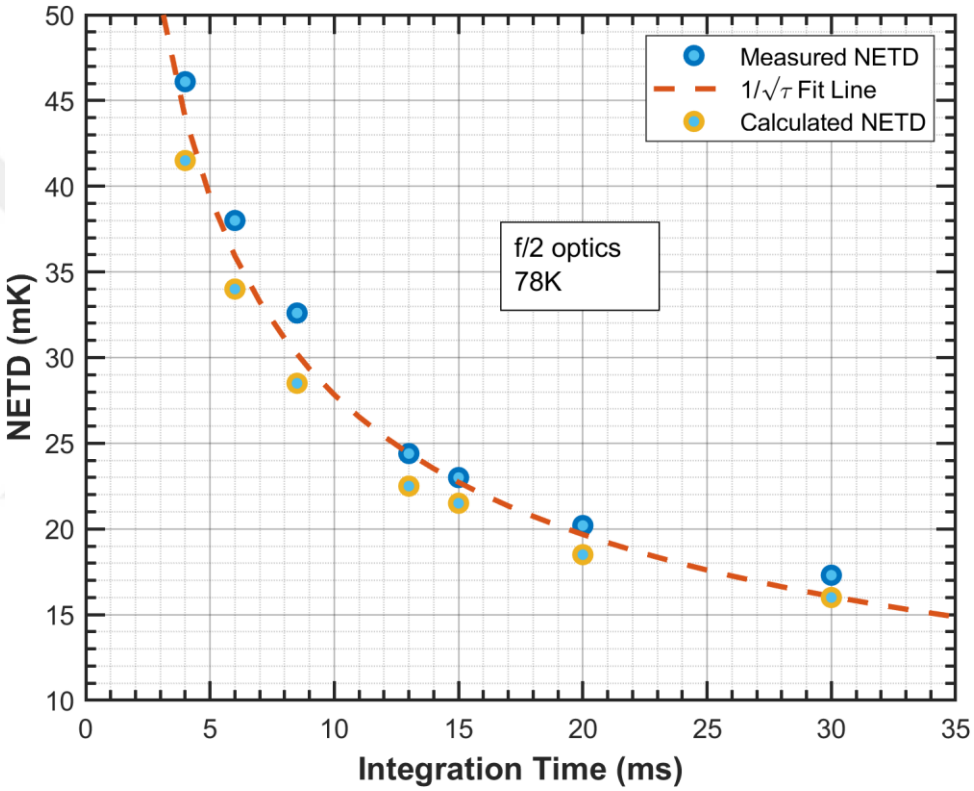

Figure 3.7 Measured and calculated NETD values of the InP/InGaAs QWIP FPA [57]

The NETD values were also calculated according to equation (3.9) where $C_{thermal}$ is thermal contrast, N_{photo} and N_{total} are the number of injected photoelectrons and total electrons respectively, g is the detector gain and n_{Read} is the electron noise of the ROIC [72]. The measured and calculated NETD values are in close relationship where measured NETD values are approximately 10% higher.

$$NETD = \frac{1}{C_{thermal} N_{photo}} \sqrt{2gN_{total} + n_{Read}^2} \quad (3.9)$$

From Figure 3.8 to Figure 3.14, NETD histograms of the operable pixels are presented at various integration times and operating temperature of 78 K with hall-filled ROIC capacitors and f/2 optics. Figure 3.15 shows image recorded by InP/InGaAs FPA at 78 K and 20 ms integration time

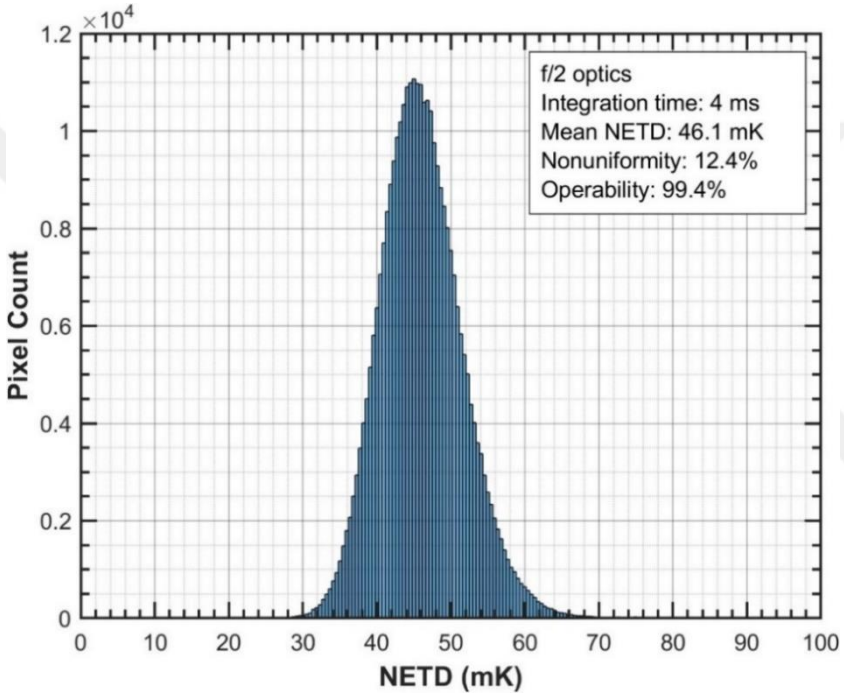

Figure 3.8 NETD histogram of the operable pixels of the InP/$In_{0.85}Ga_{0.15}As$ QWIP FPA at 4 ms integration time and at 78 K

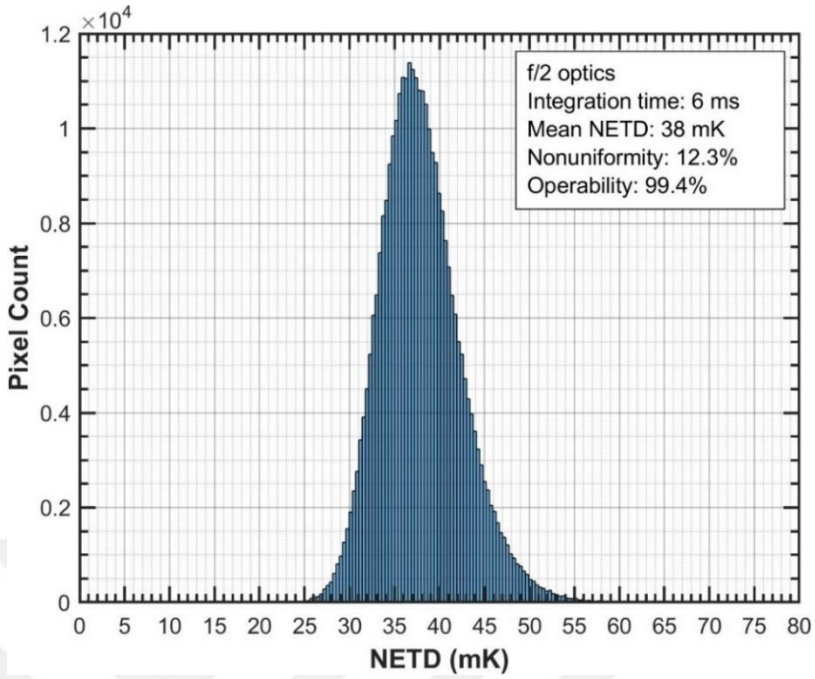

Figure 3.9 NETD histogram of the operable pixels of the InP/$In_{0.85}Ga_{0.15}As$ QWIP FPA at 6 ms integration time and at 78 K

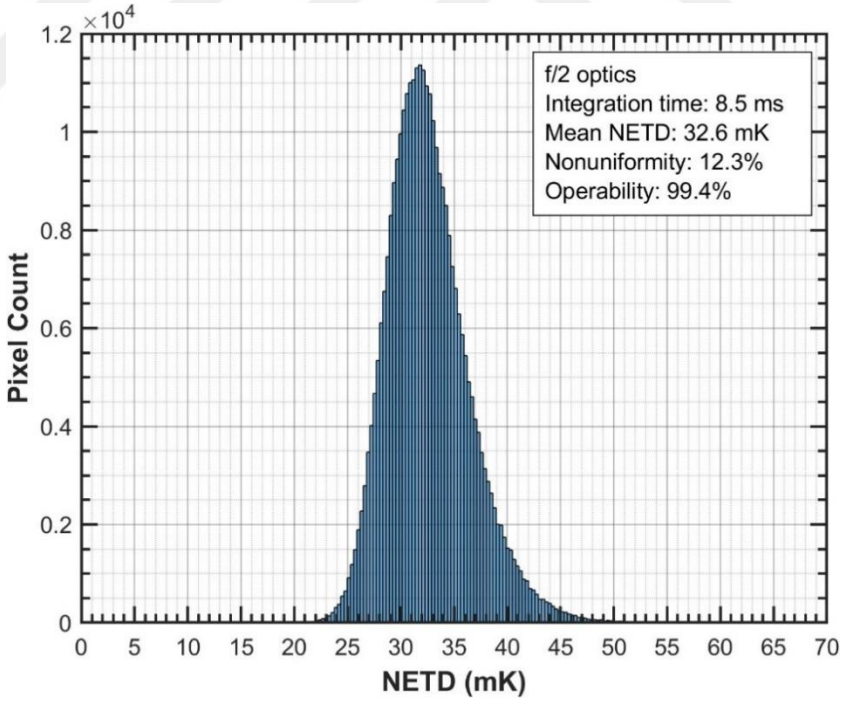

Figure 3.10 NETD histogram of the operable pixels of the InP/$In_{0.85}Ga_{0.15}As$ QWIP FPA at 8.5 ms integration time and at 78 K

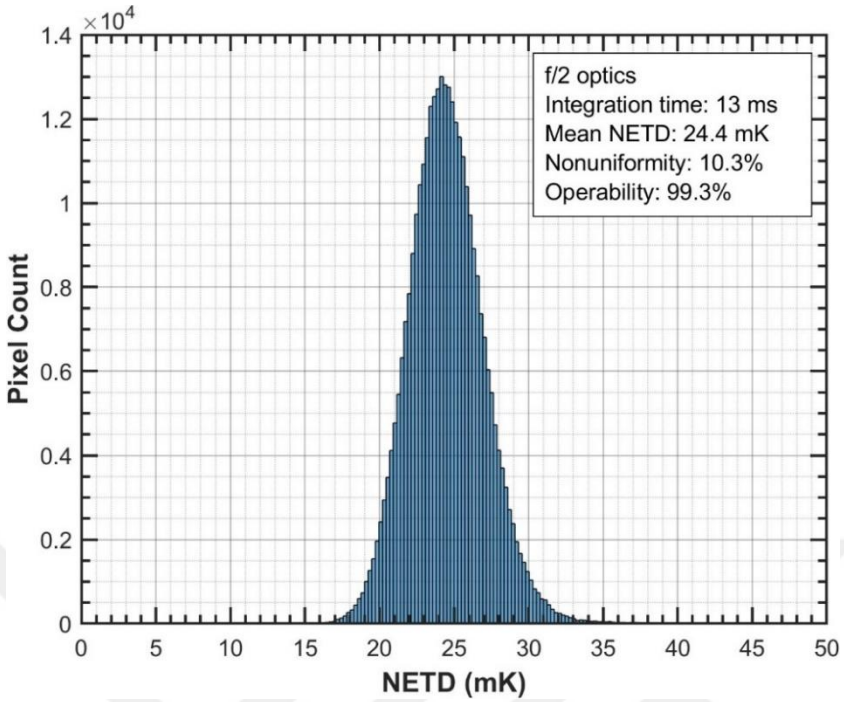

Figure 3.11 NETD histogram of the operable pixels of the InP/$In_{0.85}Ga_{0.15}As$ QWIP FPA at 13 ms integration time and at 78 K

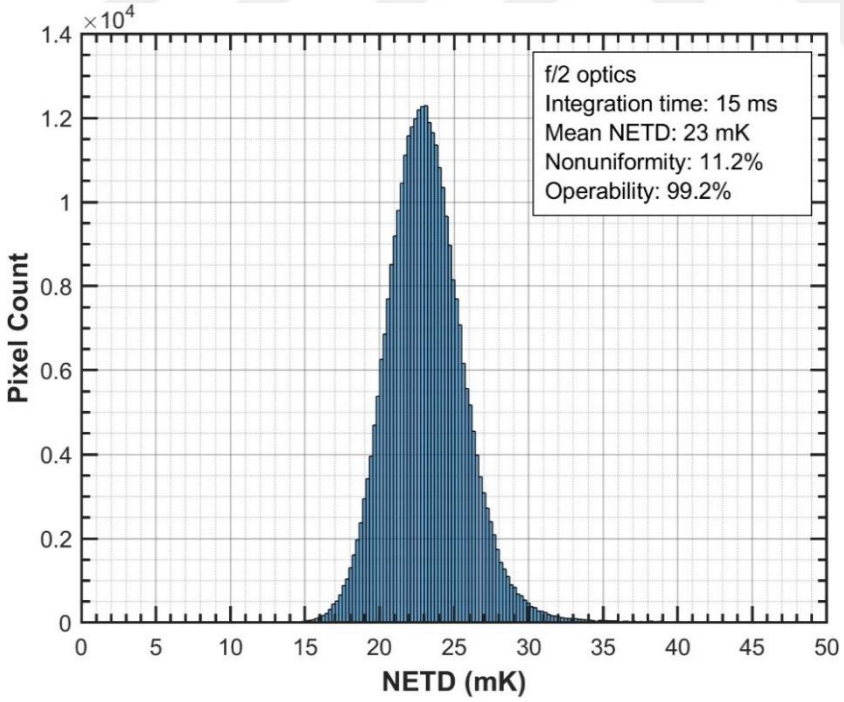

Figure 3.12 NETD histogram of the operable pixels of the InP/$In_{0.85}Ga_{0.15}As$ QWIP FPA at 15 ms integration time and at 78 K

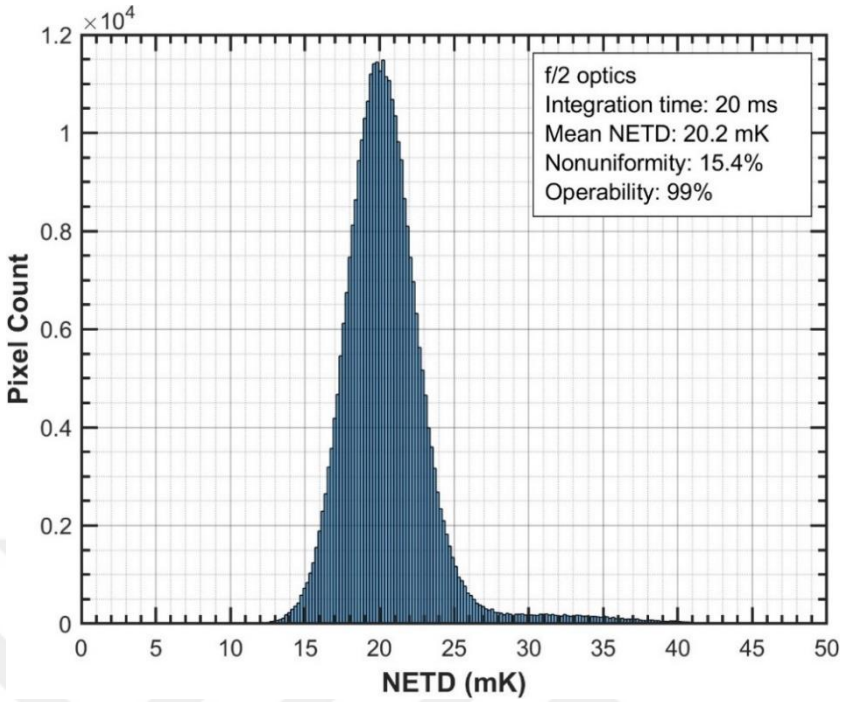

Figure 3.13 NETD histogram of the operable pixels of the InP/$In_{0.85}Ga_{0.15}As$ QWIP FPA at 20 ms integration time and at 78 K

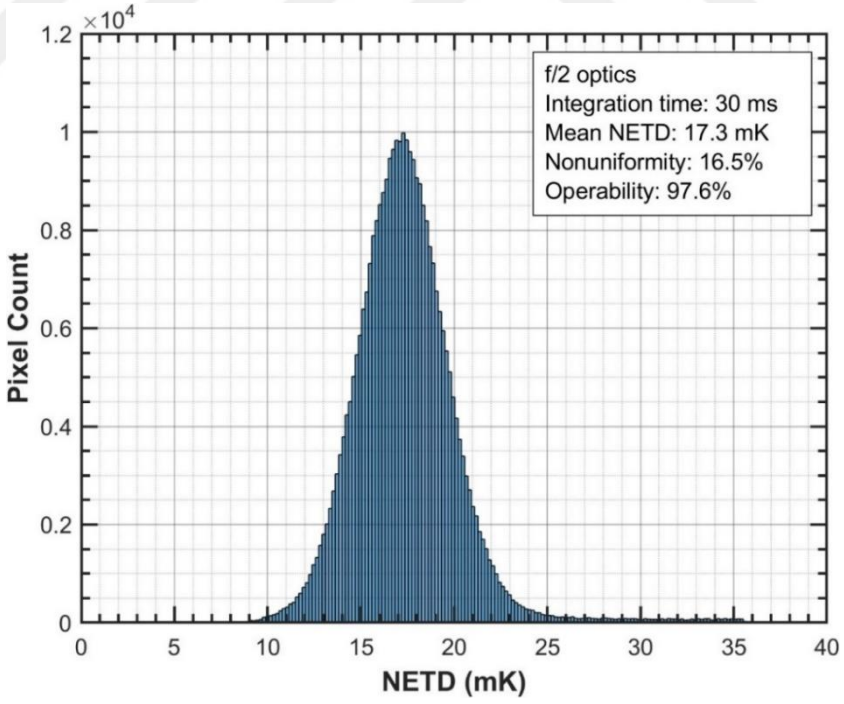

Figure 3.14 NETD histogram of the operable pixels of the InP/$In_{0.85}Ga_{0.15}As$ QWIP FPA at 30 ms integration time and at 78 K

Figure 3.15 A snapshot recorded by InP/InGaAs FPA at 78 K and 20 ms integration time [57]

3.7.2 Correctability of the InP/InGaAs QWIP FPA

Signal levels of 300 K frame for each pixel for 6 ms integration time before and after calibration are shown in Figure 3.16. The DC signal nonuniformity before calibration and after two-point NUC of the InP/InGaAs FPA is 4.76% which is less than DC signal nonuniformity of lattice-matched AlInAs/InGaAs QWIP which exhibited 6.4% nonuniformity [73]. A very high uniformity is obtained after calibration of the FPA which shows the linear approximation is valid for the correction.

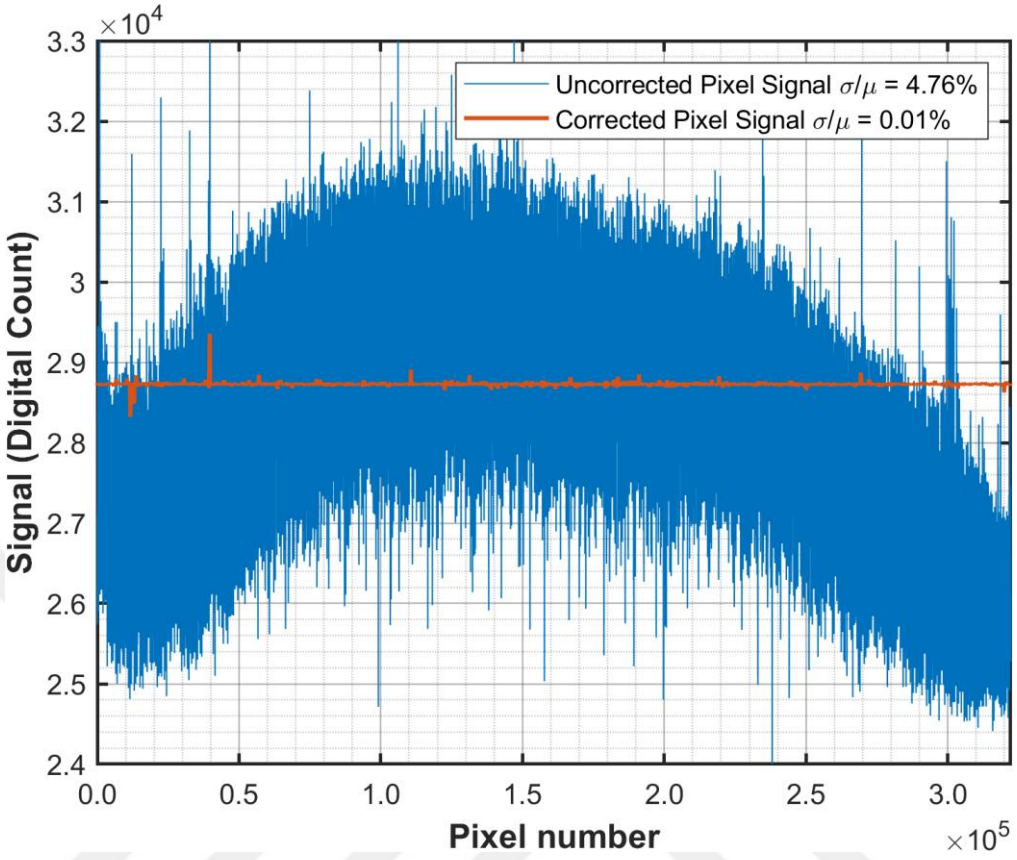

Figure 3.16 Signal level of 300 K frame at 6 ms integration time and 78 K

The correctability results are shown in Table 3.2 for calibration at 295 K, 305 K and evaluation at 300 K. For all integration times, the correctability is smaller than 1 which means that spatial noise is smaller than the temporal noise of the FPA and the calibration is valid.

Table 3.2 Correctability of the InP/InGaAs MWIR QWIP FPA

Integration time (ms)	Correctability (c)
4.0	0.1823
6.0	0.2066
8.5	0.2843
13.0	0.2821
15.0	0.2825
20.0	0.3697
30.0	0.4033

3.7.3 RTS Noise Evaluation of the InP/InGaAs QWIP FPA

In order to find the pixels exhibiting RTS noise in the InP/InGaAs QWIP FPA, with 14-bit imager, 2000 frames were taken at 5.76 Hz with integration time of 6 ms and the blackbody was set to 25 ^{o}C. Pixels exhibiting high standard deviation in time were considered as candidate pixels which might exhibit RTS noise. Those pixels were noted down and time domain signal values of each of them were inspected visually. Among 327680 pixels, only 14 pixels exhibited RTS noise in InP/InGaAs QWIP FPA. Two examples of signals in time domain and associated histograms are shown in Figure 3.17, Figure 3.18, Figure 3.19, and Figure 3.20.

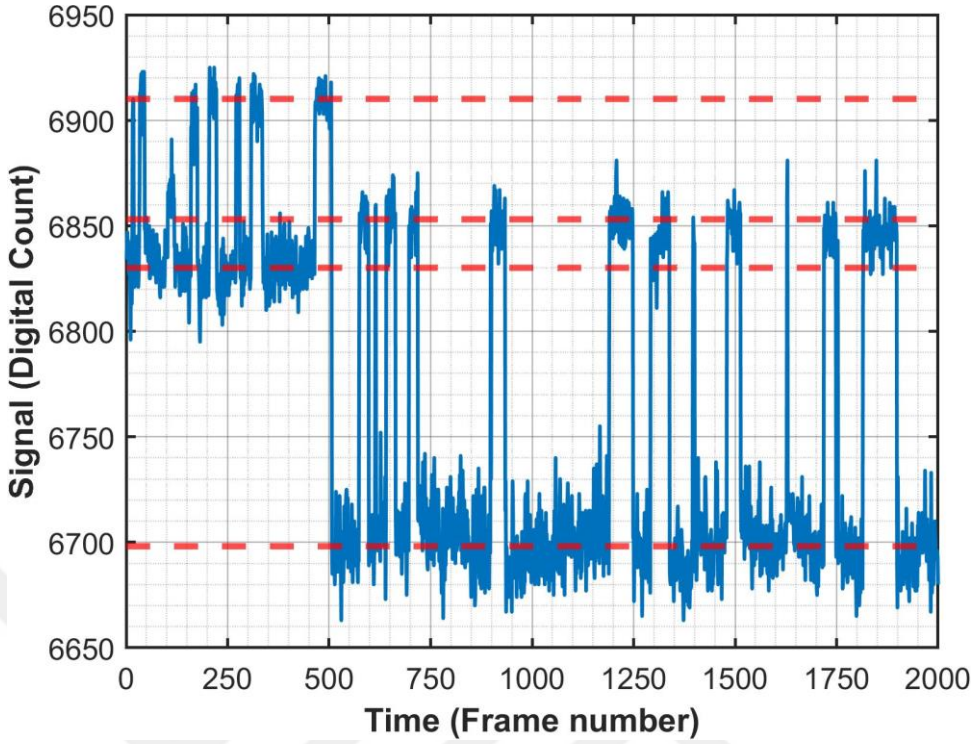

Figure 3.17 A pixel exhibiting 4 level RTS noise

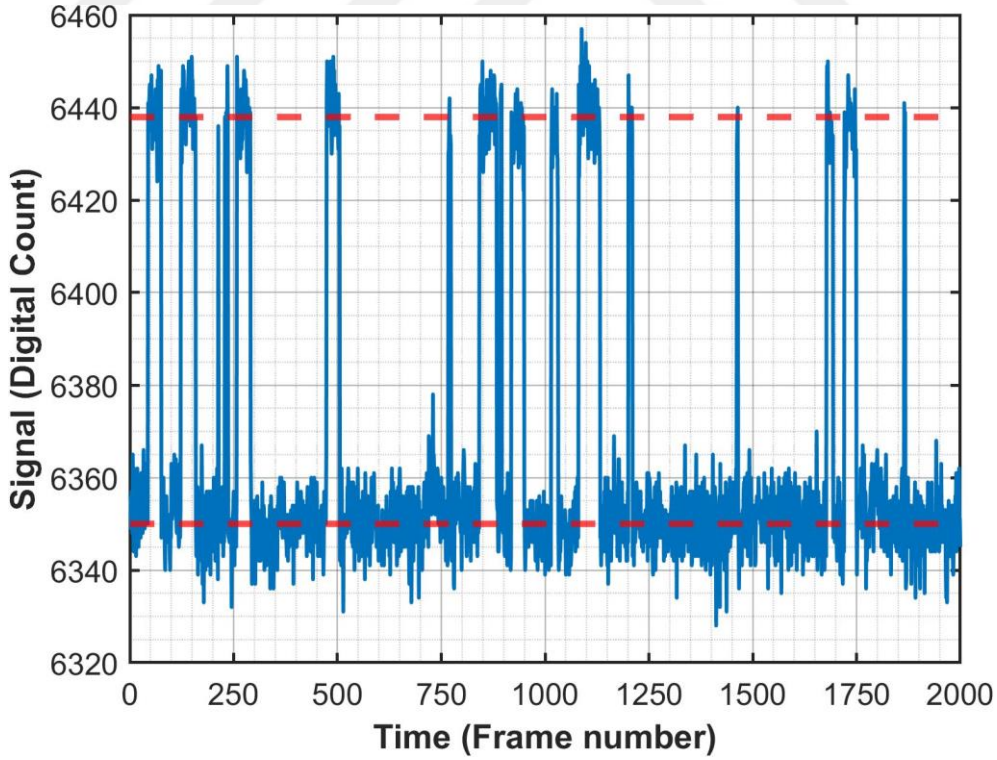

Figure 3.18 A pixel exhibiting 2 level RTS noise

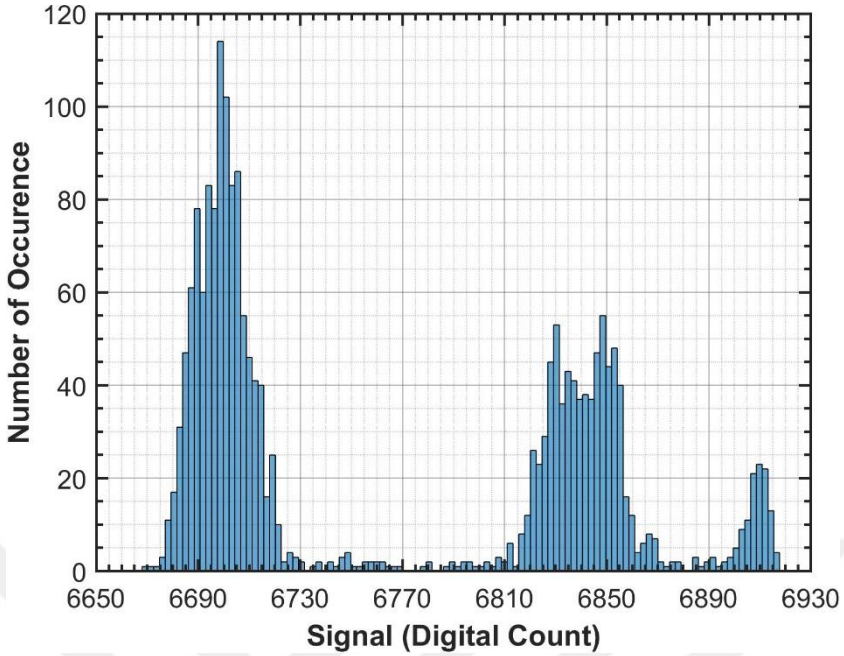

Figure 3.19 Histogram of a pixel exhibiting 4 level RTS noise in 2000 frames

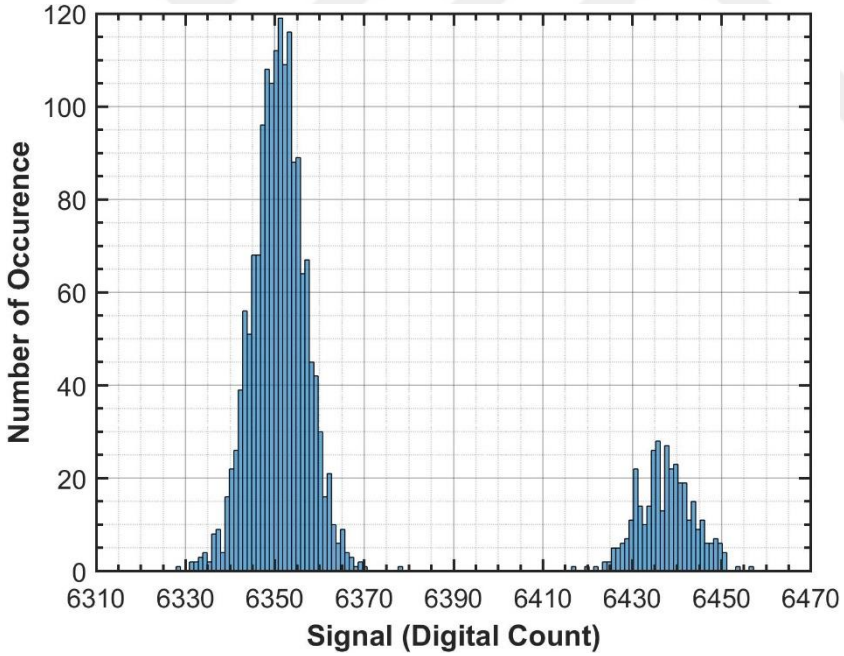

Figure 3.20 Histogram of a pixel exhibiting 2 level RTS noise in 2000 frames

It is not clear yet whether the RTS noise is created by the FPA or ROIC pixels, however, this study shows that RTS noise is not a considerable issue in the strained high-x InP/$In_xGa_{1-x}As$ QWIP technology.

3.8 Characteristics of the InP/InAs MWIR QWIP FPA

3.8.1 NETD of the InP/InAs QWIP FPA

The NETD results are presented in Figure 3.21. The NETD of characterized FPA in this study was calculated at different integration times with 14-bit imager. Although anti-reflection coating was not applied, FPA exhibited approximately 27.8 mK mean NETD with f/1.67 optics at 10 ms integration time. Assuming that 30% percent of radiation was reflected from the surface of the FPA, up to 20% improvement in NETD is also expected for this FPA when AR coating is applied.

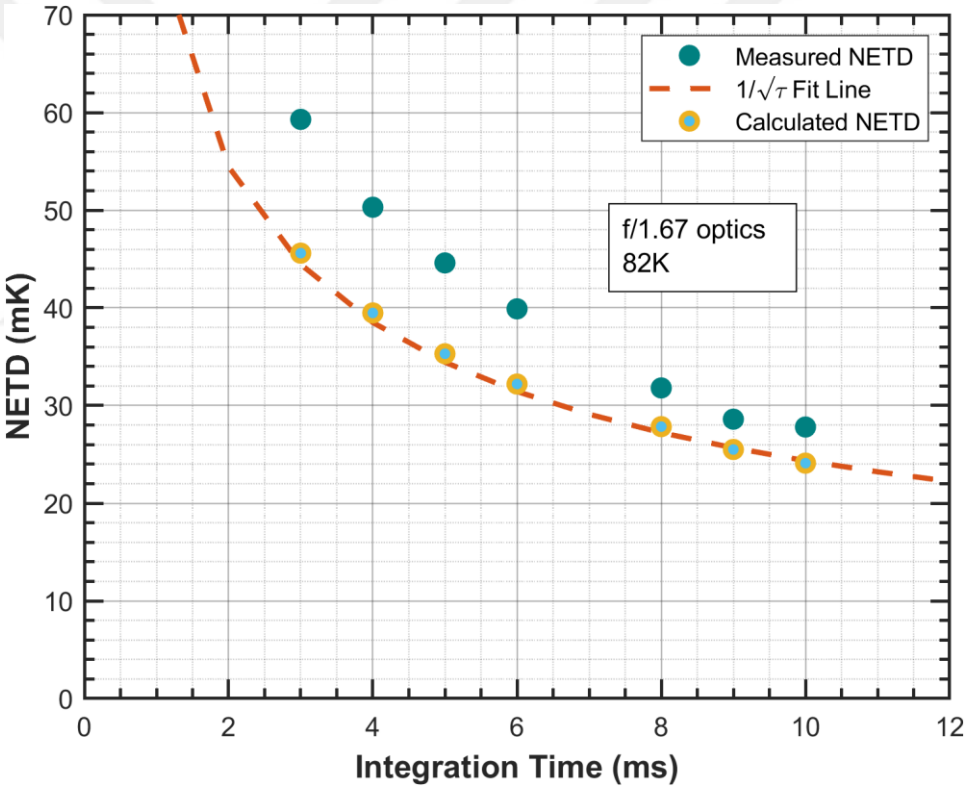

Figure 3.21 Measured and calculated NETD values of the InP/InAs QWIP FPA

From Figure 3.22 to Figure 3.28, NETD histograms of the operable pixels are presented at various integration time and operating temperature of 82 K with f/1.67 optics.

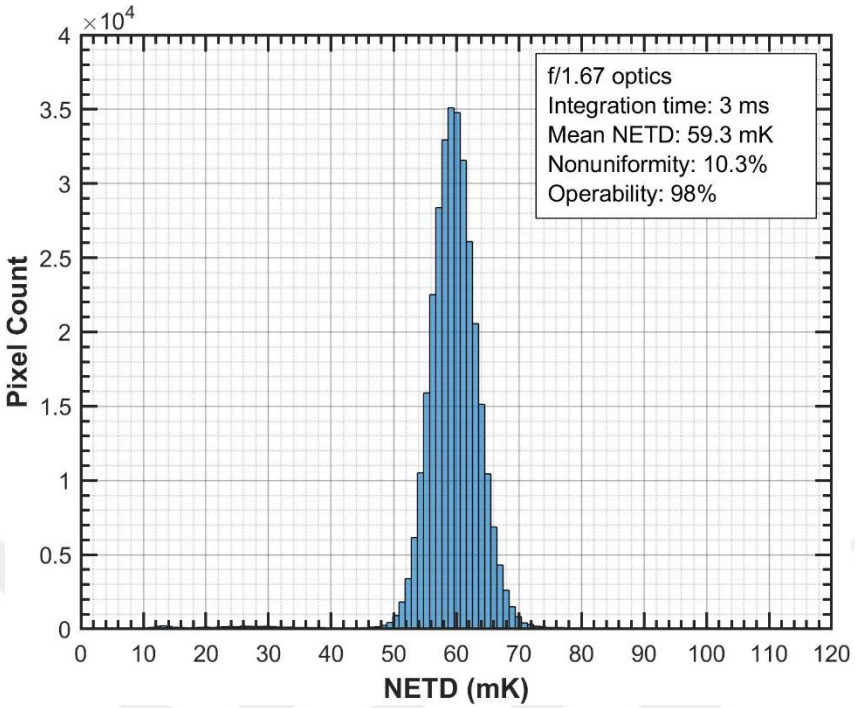

Figure 3.22 NETD histogram of the operable pixels of the InP/InAs QWIP FPA at 3 ms integration time and at 82 K

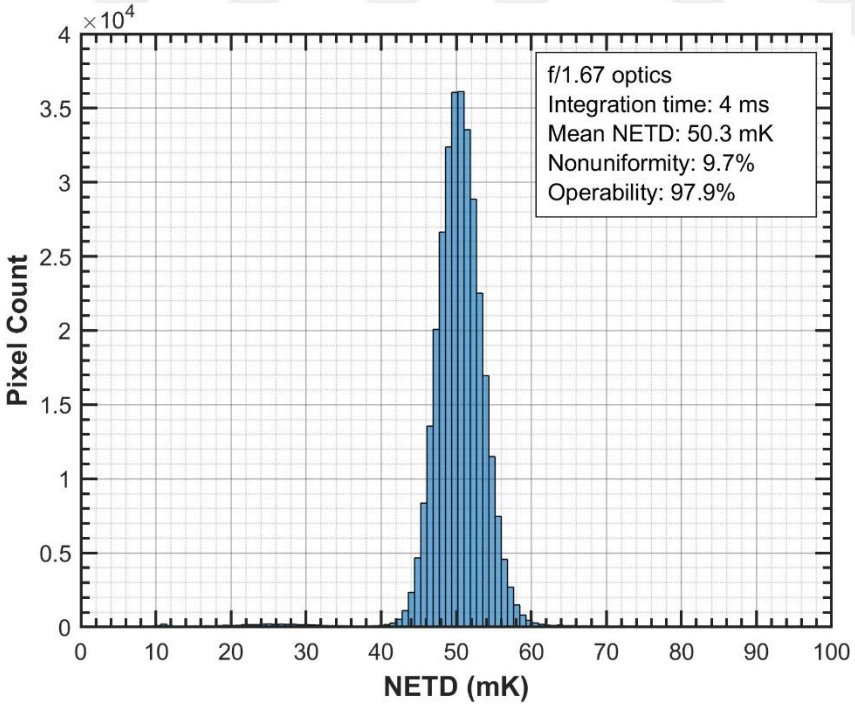

Figure 3.23 NETD histogram of operable pixels of the InP/InAs QWIP FPA at 4 ms integration time and at 82 K

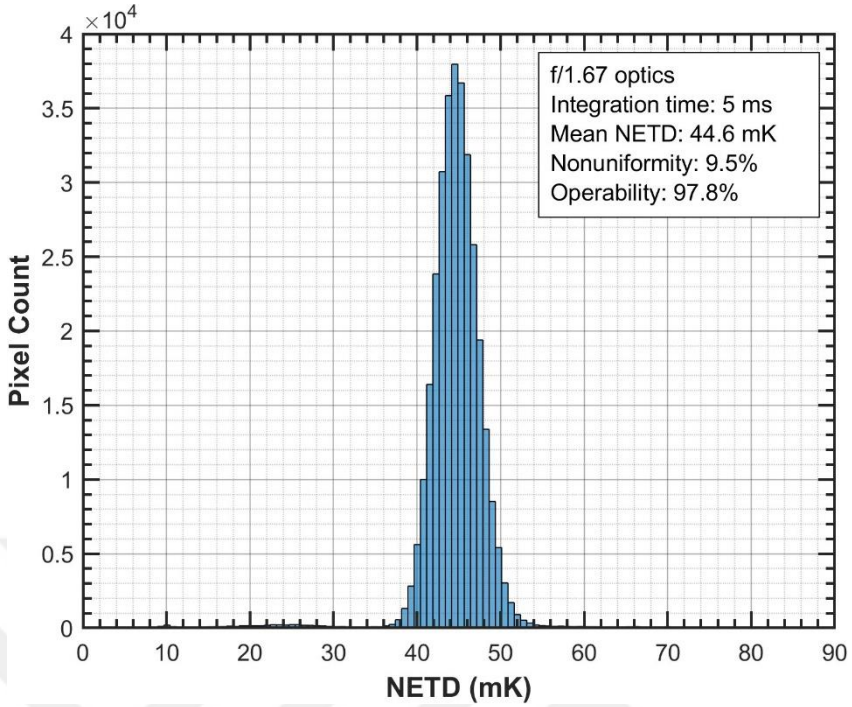

Figure 3.24 NETD histogram of operable pixels of the InP/InAs QWIP FPA at 5 ms integration time and at 82 K

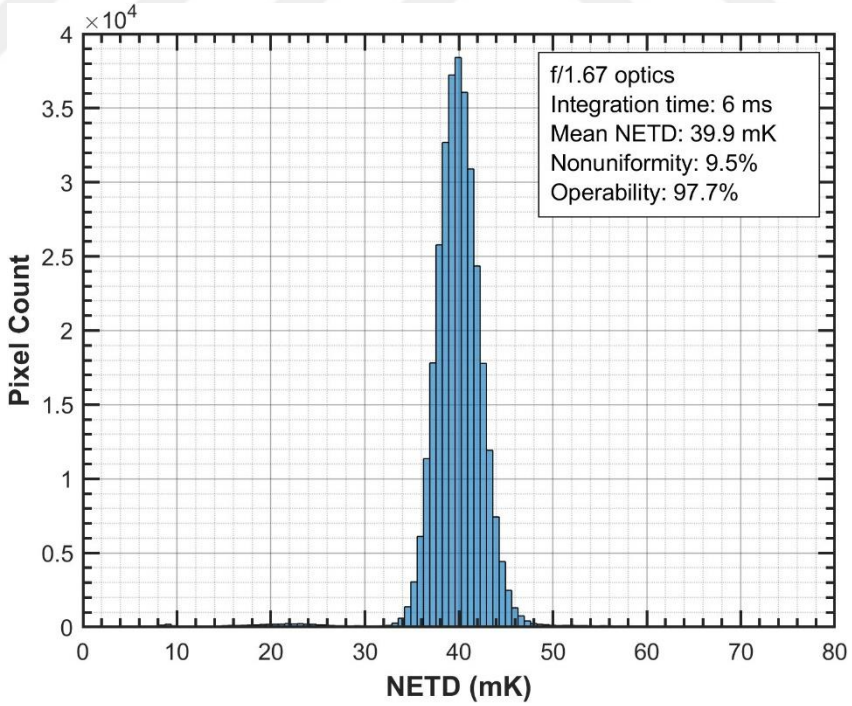

Figure 3.25 NETD histogram of operable pixels of the InP/InAs QWIP FPA at 6 ms integration time and at 82 K

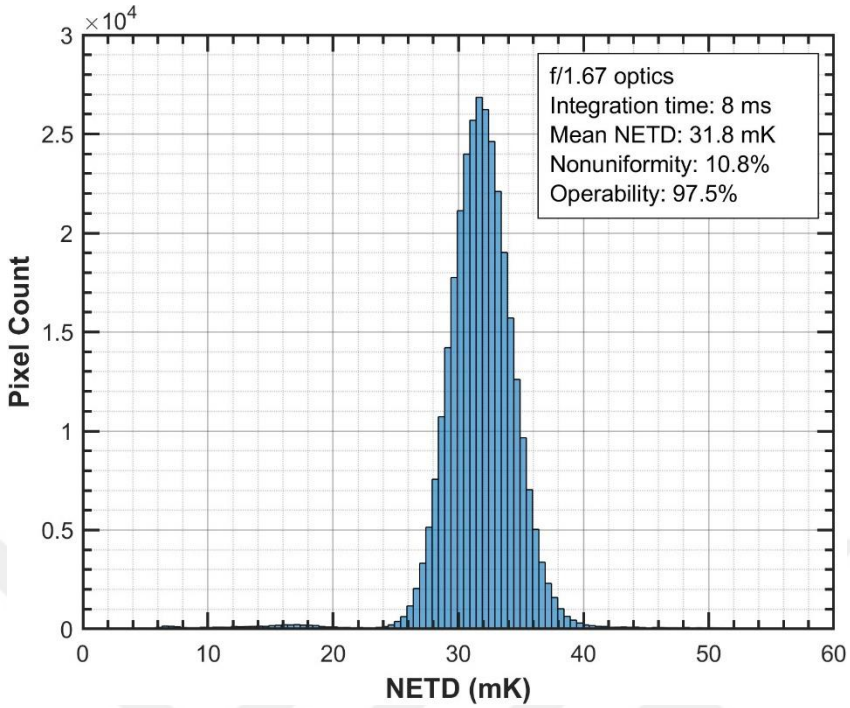

Figure 3.26 NETD histogram of operable pixels of the InP/InAs QWIP FPA at 8 ms integration time and at 82 K

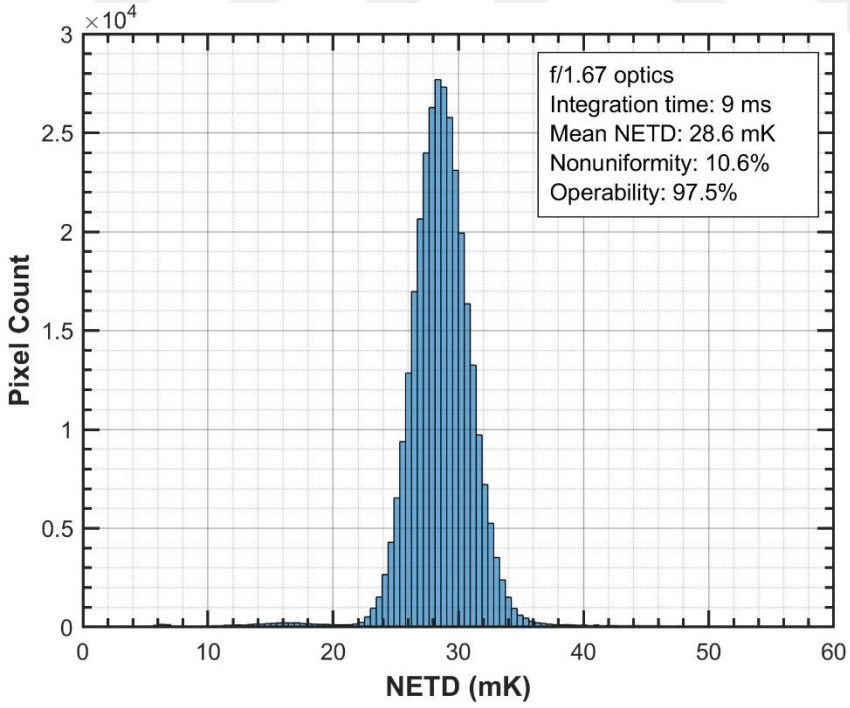

Figure 3.27 NETD histogram of operable pixels of the InP/InAs QWIP FPA at 9 ms integration time and at 82 K

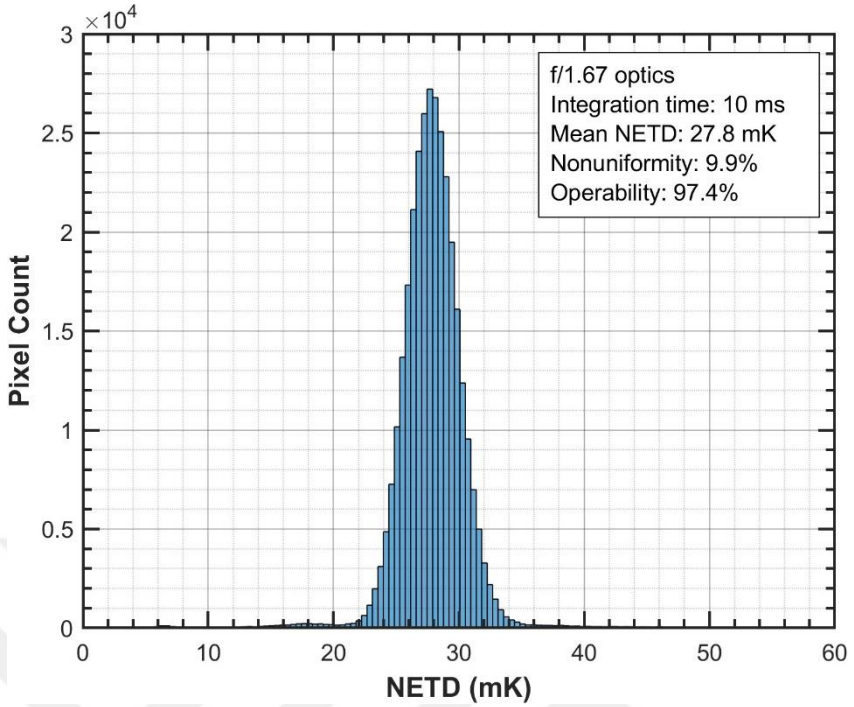

Figure 3.28 NETD histogram of operable pixels of the InP/InAs QWIP FPA at 10 ms integration time and at 82 K

The operability of the InP/InAs FPA is around 98% and the origin of the bad pixels is mostly fabrication-oriented defects (not related with the detector material). On the other hand, the calculated nonuniformities do not show the actual values for this FPA because some pixels exhibit higher response due to the fact that underfill was not distributed with perfect uniformity between the FPA and the ROIC. Therefore, NETD nonuniformity was also evaluated by selecting 256x256 pixel array where distribution of underfill material is more uniform. The InP/InAs FPA offer higher NETD uniformity than InP/InGaAs FPA. The higher NETD uniformity can be attributed to the usage of binary material in the quantum well region. Figure 3.29 shows a snapshot recorded by InP/InAs FPA at 82 K and 10 ms integration time.

Table 3.3 NETD nonuniformities of the InP/InAs QWIP FPA in the 256x256 pixels region

Integration time	Nonuniformity
3 ms	7.9%
4 ms	7.8%
5 ms	7.6%
6 ms	8.0%
8 ms	9.6%
9 ms	9.7%
10 ms	9.5%

Figure 3.29 A snapshot recorded by InP/InAs FPA at 82 K and 10 ms integration time

3.8.2 Correctability of the InP/InAs QWIP FPA

The correctability results are shown in Table 3.4 for calibration at 295 K and 305 K and evaluation at 300 K for the InP/InAs QWIP FPA. For all integration times, the correctability is also smaller than 1 for this FPA.

Table 3.4 Correctability of the InP/InAs MWIR QWIP FPA

Integration time (ms)	Correctability (c)
2.17	0.2272
3.13	0.2303
4.09	0.2653
5.29	0.2682
6.02	0.2875
7.94	0.3121

3.8.3 RTS Noise Evaluation of the InP/InAs QWIP

To find the pixels exhibiting RTS noise in the InP/InAs QWIP FPA, with 14-bit imager, 2000 frames were taken at 5.76 Hz with integration time of 4 ms and the blackbody was set to 25 ^{o}C. The method used for the evaluation RTS noise of the InP/InGaAs QWIP FPA was applied to find pixels exhibiting RTS noise of the InP/InAs QWIP FPA. Among 327680 pixels, 377 pixels exhibited RTS noise. An example of signal in time domain and associated histogram are shown in Figure 3.30 and Figure 3.31. Both FPAs do not suffer from RTS. On the other hand, pixel exhibiting RTS noise should be considered as bad pixel and must be corrected to prevent blinking pixels.

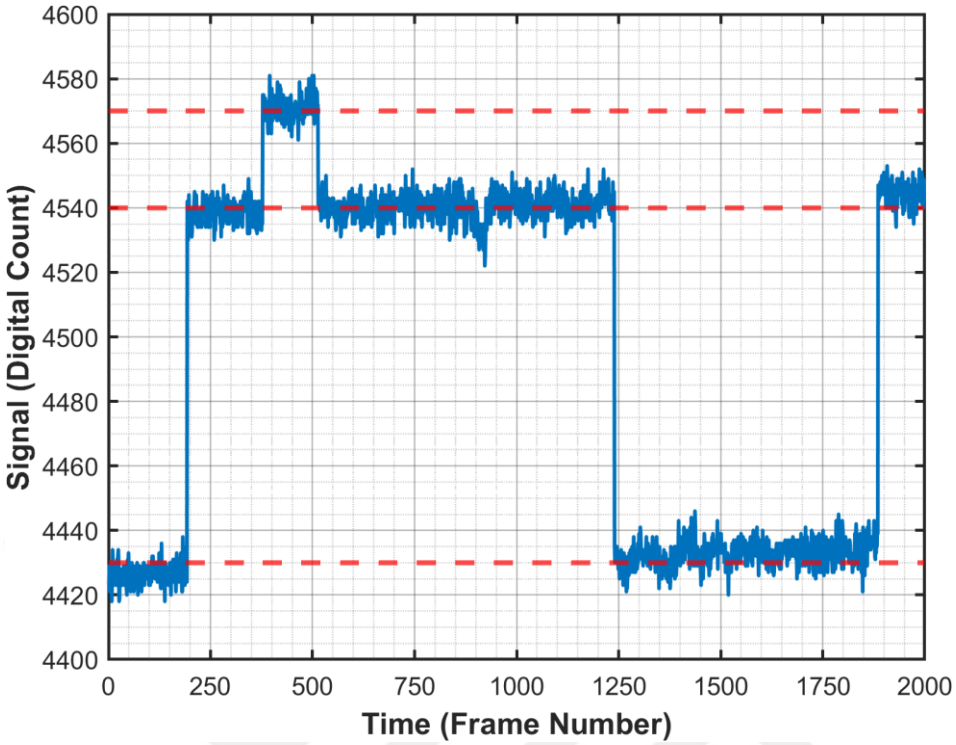

Figure 3.30 A pixel exhibiting 3 level RTS noise

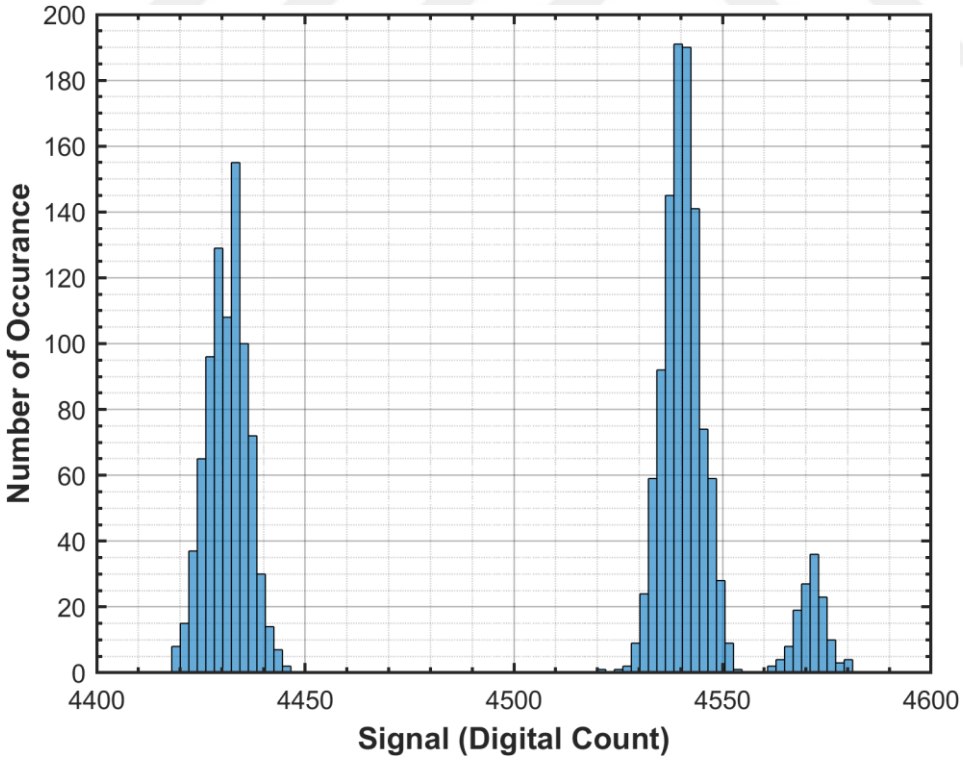

Figure 3.31 Histogram of a pixel exhibiting 3 level RTS noise in 2000 frames

This study also shows that RTS noise is not a considerable issue in the strained InP/InAs QWIP technology.

3.9 Comparison with other MWIR FPA Technologies

The FPAs (based on InP/InGaAs and InP/InAs material systems) characterized in this thesis work exhibits similar performance in terms of NETD. In order to assess the FPAs NETD performances effectively, the NETD results from literature are also presented in Table 3.5.

Table 3.5 NETD values of the MWIR FPAs based on different material technologies

Technology	**NETD (mK)**	**Optics**	**Integration Time (ms)**	**Pixel active area (μm^2)**	**Cut-off (µm)**
InP/InGaAs QWIP	**20.2**	**f/2**	**20**	**12x12**	**6.0**
InP/InAs QWIP	**27.8**	**f/1.67**	**10**	**10x10**	**6.2**
AlInAs/InGaAs QWIP [73]	22	f/1.5	20	23x23	4.9
AlGaAs/InGaAs QWIP [74]	19	f/2.5	60	17.5x17.5	5.1
AlGaAs/InGaAs QWIP - 2 [75]	14.3	f/1.5	20	22x22	5.1
HgCdTe [76]	19.6	f/4	5	13x13	5.3
InSb [77]	14.6	f/2.3	3	28x28	5.5
T2SL [78]	21	f/4	10	13x13	5.3

The NETD values should be corrected to the same level to make a fair comparison. Therefore, the optical aperture and areas of the pixels were corrected, according to Equation (1.21), to f/2 optics and 12x12 μm^2. For non-reported pixel active areas, the side lengths of the pixels were assumed to be the pitch length minus 2 µm. Reflection from the surface was also corrected, if the AR coating was not applied. The corrected NETD values are marked on integration time (τ) vs. NETD plot (Figure 3.32) where scaled $1/\sqrt{\tau}$ lines were also drawn to evaluate the corrected NETD performances for different integration times. $1/\sqrt{\tau}$ lines state that points on the same line represent similar NETD performance and lines which are closer to left side of the plot correspond to better NETD performance.

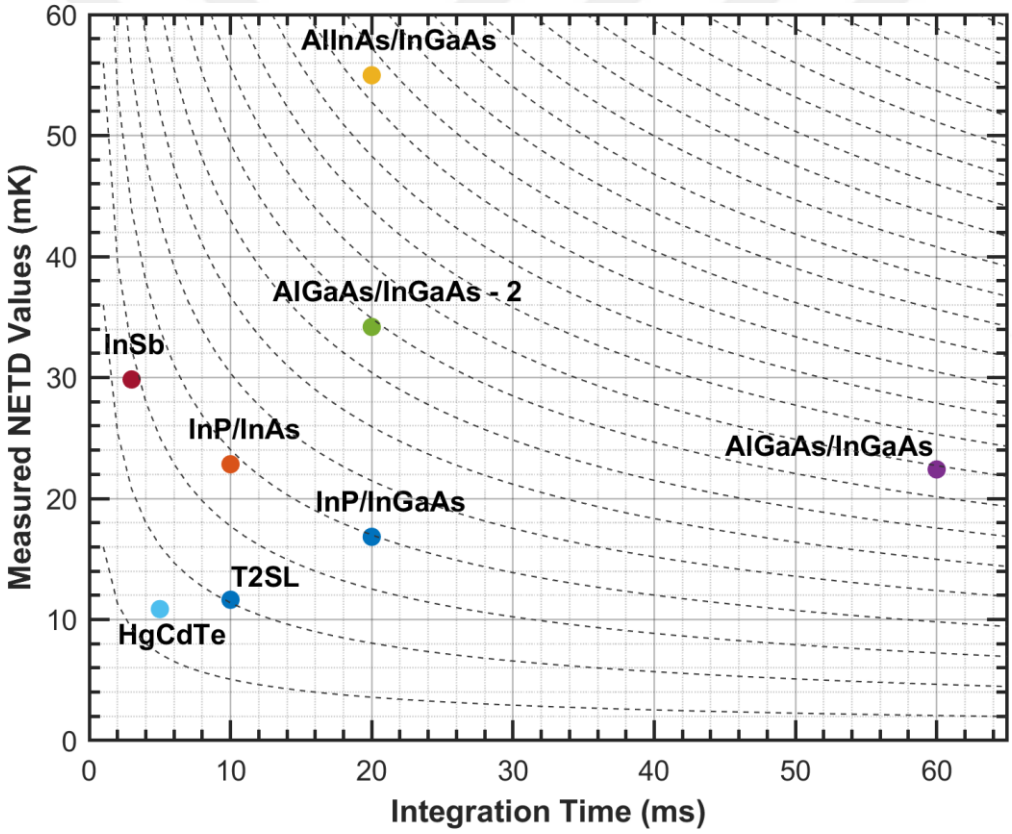

Figure 3.32 NETD vs. integration time for different MWIR FPA technologies (all values are corrected to 12x12 μm^2 active area and f/2 optic, the effect of AR coating is also corrected)

As seen from the Figure 3.32, HgCdTe, T2SL and InSb technologies offer very good NETD performance even with integration times less than 10 ms. On the other hand,

for high enough integration times InP based QWIP technology can also offer the same NETD performance. Therefore, if the application does not require very high frame rates and very low integration times (submiliseconds), InP QWIPs can be a proper alternative to the other technologies. The characterized FPAs in this thesis work offer very high uniformity thanks to the absence of diffraction grating, therefore, spatial noise does not limit the FPA performance for long integration times. Moreover, GaAs QWIP technology does not reach NETD values lower than 20 mK due to low quantum efficiency even with very high integration times. GaAs QWIP technology also may not meet pitch reduction need of new generation infrared sensor technology due to the requirement of diffraction grating which performs reduced efficiency with decreasing number of grating periods [16]. The NETD performance of the GaAs QWIP is not close the InSb. The NETD performance gap between those technologies is perfectly filled with the InP QWIP technology even without any light coupler scheme. InP technology offers widely accessible and high-quality substrates which makes the fabrication easier. This technology also offers adjustable gain property in a wide bias range. The gain of the detector can be adjusted so that high performance imaging can be performed under varying background photon flux. This feature is not provided photovoltaic based detectors due to fixed gain and standard GaAs QWIP technology because of gain saturation [79]. On the other hand, photodetectors in this thesis work can provide high and adjustable gain in a wide bias range.

In order not to suffer from spatial noise which limits the FPA performance especially for high integration times, an FPA must have low NETD nonuniformity. As seen from Table 3.6, the QWIP technology offers less nonuniformity than technologies that performs very low temporal NETD. Therefore, the performance limitation due to the varying pixel characteristics is less in QWIP based FPAs.

Table 3.6 NETD nonuniformity measurement results for different MWIR technologies

Technology	NETD Nonuniformity
InP/InGaAs QWIP	**12.0%**
InP/InAs QWIP	**8.0%**
AlGaAs/InGaAs QWIP [74]	5.5%
HgCdTe [77]	21.5%
InSb [77]	13.1%

CHAPTER 4

CONCLUSION

In this thesis study, two different 640x512 format and 15 μm pitch FPAs which are based on InP QWIP technology and operate in the MWIR band were characterized to show that InP QWIP technology offers high performance FPAs in the MWIR band. The first FPA was based on strained InP/$In_{0.85}Ga_{0.15}As$ material system and performed 20.2 mK mean NETD with 20 ms integration time and f/2 optics. The pixel active area of this FPA was 12x12 μm^2. The second FPA was based on strained InP/InAs material system. It yielded 27.8 mK mean NETD with 10 ms integration time, f/1.67 optics and pixel active area was 10x10 μm^2. Both FPAs exhibited very low NETDs without AR coating and diffraction grating.

It is shown that if the imaging application does not require very low integration times, InP/$In_{0.85}Ga_{0.15}As$ and InP/InAs QWIPs can also be a proper IR detector for thermal imaging applications in the MWIR band thanks to the high enough conversion efficiency of high-x InP/$In_xGa_{1-x}As$.

Both FPAs characterized in this thesis work were free of diffraction grating. This shows that high-x InP/$In_xGa_{1-x}As$ QWIP technology offers high performance without requirement of any light coupling scheme.

Although the material systems were strained for both FPAs, they performed very high uniformity with correctable performances. The NETD nonuniformities of the InP/$In_{0.85}Ga_{0.15}As$ and InP/InAs QWIP FPAs were 10.3% and 8.0% for 13 ms and 6 ms integration times, respectively. The lower nonuniformity in the InP/InAs QWIP FPA can be attributed to the usage of binary material in the well region. The strain did not also cause any stability problem. The number of pixels showing RTS noise was not at considerable level in both FPAs.

It is deduced that GaAs QWIP technology suffers from low conversion efficiency and cannot offer low NETD with small pitches even with integration times of 30 ms. Due to the gain saturation in GaAs QWIP technology, GaAs based QWIP cannot offer adjustable gain for different bias voltages, on the other hand, variable gain feature of the InP technology makes the FPA adaptable for altering scene conditions.

The mature fabrication nature of InP technology enables inexpensive fabrication with high yields. Easily reachable high quality InP substrates makes the fabrication sustainable and easier.

All in all, high-x InP/$In_xGa_{1-x}As$ QWIP technology offers high performance in the MWIR band and can be an alternative to other IR detector technologies. This technology also overcomes the two main limitations which are the requirement of diffraction grating and low conversion efficiency of the standard QWIP technology. High-x InP/$In_xGa_{1-x}As$ QWIP technology provides high enough conversion efficiency allowing operability in low background conditions or high frame rates.

For the future work, the cut-off wavelength of the detector can be reduced to around 5 μm, to make long distance imaging more effective and increase the operating temperature of the detectors. This can be accomplished by optimizing the epilayer structure. Well and barrier materials can be optimized to create larger energy difference between quantized energy states.

REFERENCES

[1] J. R. Fleming, Historical Perspectives on Climate Change, New York: Oxford University Press, 1998, p. 64.

[2] M. Rowan-Robinson, Night Vision: Exploring the Infrared Universe, New York: Cambridge University Press, 2013, p. 23.

[3] A. Rogalski, "History of infrared detectors," *Opto-Electronics Review,* vol. 20, no. 3, pp. 279-308, 2012.

[4] B. Levine, K. Choi, C. Bethea, J. Walker and R. Malik, "New 10 μm Infrared Detector Using Intersubband Absorption in Resonant Tunneling GaAlAs Superlattices," *Applied Physics,* vol. 50, no. 16, pp. 1092-1094, 1987.

[5] A. Rogalski, Infrared Detectors, S.l.: CRC PRESS, 2010.

[6] A. Daniels, Field Guide to Infrared Systems, Bellingham: SPIE Press, 2007.

[7] D. J. Lockwood, "Encyclopedia of Color Science and Technology," in *Rayleigh and Mie Scattering*, New York, Springer New York, 2016, pp. 1097-1107.

[8] A. Rogalski and K. Chrzanowski, "Infrared Devices and Techniques," *Opto-electronics Review,* vol. 10, pp. 111-136, 2002.

[9] A. Rogalski, "Comparison of photon and thermal detector performance," in *Handbook of Infra-red Detection Technologies,* Elsevier Science, 2002, pp. 5-81.

[10] P. W. Kruse, "A comparison of the limits to the performance of thermal and photon detector imaging arrays," *Infrared Physics & Technology,* vol. 36, no. 5, pp. 869-882, 1995.

[11] S. B. S. Ardebili, J. S. Kim, J. Ha, T. I. Kang, B. Z. Farzin, Y. Kim and S. J. Lee, "Band-to-band transitions in InAs/GaSb Multi-Quantum-Well structures using K.P theory: Effects of well/barrier width and temperature," *Energies,* vol. 16, no. 3, p. 1162, 2023.

[12] R. A. T. Santos, F. D. P. Alves, C. G. R. Taranti, L. A. Faria and A. A. Quivy, "Quantum well infrared photodetector design using Transfer Matrix Method," *2009 SBMO/IEEE MTT-S International Microwave and Optoelectronics Conference (IMOC),* pp. 316-320, 2009.

[13] L. Stabellini, W. Lu, A. D. Rossi, T. Antoni, M. Carras, S. Trillo and G. Bellanca, "An FDTD approach to the simulation of quantum-well infrared photodetectors," *Optical and Quantum Electronics,* vol. 40, pp. 1085-1090, 2008.

[14] Y. Fu, M. Willander, W. Lu and W. Xu, "Optical coupling in quantum well infrared photodetector by diffraction grating," *Journal of Applied Physics,* vol. 84, p. 5750–5755, 1998.

[15] C. Besikci, "High-x InP/$In_xGa_{1-x}As$ quantum well infrared photodetector," *Infrared Physics & Technology,* vol. 95, pp. 152-157, 2018.

[16] C. Besikci and S. V. Balcı, "Diffraction-Grating-Free Very Small-Pitch High-x InP/In_xGa_{1-x} as Quantum Well Infrared Photodetectors," *IEEE Electron Device Letters,* vol. 43, no. 8, pp. 1287-1290, 2022.

[17] A. Rogalski, "Infrared detectors: status and trends," *Progress in Quantum Electronics,* vol. 27, no. 2-3, pp. 59-210, 2003.

[18] E. A. Plis, "InAs/GaSb Type-II Superlattice Detectors," *Advances in Electronics,* vol. 2014, pp. 1-12, 2014.

[19] C.-J. H. G. D. S. Chuan C. Li, "Overview of DRS uncooled VOx infrared detector development," *Optical Engineering,* vol. 50, no. 6, 2011.

[20] J. D. Vincent, Fundamentals of Infrared and Visible Detector Operation and Testing, Wiley-VCH, 1990.

[21] Y. Arslan, "High Performance Focal Plane Array Technologies From Short To Long Wavelength Infrared Bands," Ph. D. Thesis, Middle East Technical University, 2014.

[22] J.D.Vincent, Fundamentals of Infrared Detector Operation and Testing, New York: Wiley, 1990.

[23] B. F. Levine, C. G. Bethea, K. G. Glogovsky, J. W. Stayt and R. E. Leibenguth, "Long-wavelength 128x128 GaAs quantum well infrared photodetector," *Semiconductor Science and Technology,* vol. 6, pp. 114-119, 1991.

[24] L. J. Kozlowski, G. M. Williams, G. J. Sullivan, C. W. Farley, R. J. Anderson, J. Chen, D. T. Cheung, W. E. Tennant and R. E. DeWames, "LWIR 128x128 GaAs/AlGaAs multiple quantum well hybrid focal plane array," *IEEE Transactions on Electron Devices,* vol. 38, pp. 1124-1130, 1991.

[25] O. O. Cellek, "Ensemle Monte Carlo Simulation Of Quantum Well Infrared Photodetecors, And InP Based Long Wavelength Quantum Well Infrared Photodetectors For Thermal Imaging," Ph. D. Thesis, Middle East Technical University, 2006.

[26] H. Schneider and H. C. Liu, Quantum Well Infrared Photodetectors, Heidelberg: Springer Berlin, 2007.

[27] L. C. West and S. J. Eglash, "First observation of an extremely large-dipole infrared transition within the conduction band of a GaAs quantum well," *Applied Physics Letters,* vol. 46, pp. 1156-1158, 1985.

[28] J. Piprek, Handbook of Optoelectronic Device Modeling and Simulation, Boca Raton: CRC Press, 2021.

[29] M. Z. Tidrow, "QWIP and MCT for Long Wavelength and Multicolor Focal Plane Array Applications," Army Research Laboratory, Washington, 1997.

[30] S. Özer, "InSb and InAsSb Infrared Photodiodes on Alternative Subtrates and InP/InGaAs Quantum Well Infrared Photodetectors: Pixel and Focal Plane Array Performance," Ph. D. Thesis, Middle East Technical University, 2005.

[31] K. K. Choi, B. F. Levine, R. J. Malik, J. Walke and C. G. Bethea, "Periodic negative conductance by sequential resonant tunneling through an expanding high-field superlattice domain," *Physical Review B,* vol. 35, pp. 4172-4175, 1987.

[32] B. F. Levine, "Quantum-well infrared photodetectors," *Journal of Applied Physics,* vol. 74, no. 8, pp. R1-R81, 1993.

[33] G. Hasnain, B. F. Levine, S. Gunapala and N. Chand, "Large photoconductive gain in quantum well infrared photodetectors," *Applied Physics Letters,* vol. 57, no. 6, pp. 608-610, 1990.

[34] O. O. Cellek and C. Besikci, "Detailed investigation of electron transport, capture and gain in Al0.3Ga0.7As/GaAs quantum well infrared

photodetectors," *Semiconductor Science and Technology,* vol. 19, no. 2, pp. 183-190, 2003.

[35] G. Torunoğlu, "Fabrication and Characterization of InP based Quantum Well Infrared Photodetectors," M. Sc. Thesis, Middle East Technical University, 2012.

[36] K. Choi, D. Forrai, D. Endres, J. Sun, P. Pinsukanjana and J. Devitt, "C-QWIP focal plane arrays," *Infrared Physics & Technology,* vol. 52, no. 6, pp. 364-370, 2009.

[37] B. F. Levine, S. D. Gunapala and R. F. Kopf, "Photovoltaic GaAs quantum well infrared detectors at 4.2 μm using indirect Al_xGa_{1-x} barriers," *Applied Physics Letters,* vol. 58, no. 14, pp. 1551-1553, 1991.

[38] A. G. U. Perera, W. Z. Shen, S. G. Matsik, H. C. Liu, M. Buchanan and W. J. Schaff, "GaAs/AlGaAs quantum well photodetectors with a cutoff wavelength at 28 μm," *Applied Physics Letters,* vol. 72, no. 13, pp. 1596-1598, 1998.

[39] K. K. Choi, S. V. Bandara, S. D. Gunapala, W. K. Liu and J. M. Fastenau, "Detection wavelength of InGaAs/AlGaAs quantum wells and superlattices," *Journal of Applied Physics,* vol. 91, no. 2, p. 551–564, 2002.

[40] M. Sundaram and S. C. H. Wang, "Two-color QWIP FPAs," *Proceedings of SPIE-Infrared Detectors and Focal Plane Arrays VI,* vol. 4028, pp. 311-317, 2000.

[41] M. Z. Tidrow, X. Jiang, S. S. Li and K. Bacher, "A four-color quantum well infrared photodetector," *Applied Physics Letters,* vol. 74, no. 9, pp. 1335-1337, 1999.

[42] M. Kaldırım, "Dual And Single Color Mid-wavelength Infrared Quantum Well Photodetectors," M. Sc. Thesis, Middle East Technical University, 2008.

[43] O. O. Cellek, S. Ozer and C. Besikci, "High responsivity InP-InGaAs quantum-well infrared photodetectors: characteristics and focal plane array performance," *IEEE Journal of Quantum Electronics,* vol. 41, no. 7, pp. 980-985, 2005.

[44] Y. Gusakov, E. Finkman, G. Bahir and D. Ritter, "The effect of strain in InP/InGaAs quantum-well infrared photodetectors on the operating wavelength," *Applied Physics Letters,* vol. 79, no. 16, pp. 2508-2510, 2001.

[45] Y. Arslan, T. Colakoglu and C. Besikci, "Diffraction-Grating-Coupled High Quantum Efficiency InP/InGaAs Quantum Well Infrared Photodetector Focal Plane Array," *IEEE Journal of Quantum Electronics,* vol. 49, no. 2, pp. 186-195, 2013.

[46] S. D. Gunapala, B. F. Levine, D. Ritter, R. A. Hamm and M. B. Panish, "Lattice-matched InGaAsP/InP long-wavelength quantum well infrared photodetectors," *Applied Physics Letters,* vol. 60, no. 5, pp. 636-638, 1992.

[47] C. Besikci, "Nature Allows High Sensitivity Thermal Imaging With Type-I Quantum Wells Without Optical Couplers: A Grating-Free Quantum Well Infrared Photodetector With High Conversion Efficiency," *IEEE Journal of Quantum Electronics,* vol. 57, no. 2, pp. 1-12, 2021.

[48] S. D. Gunapala, S. V. Bandara, J. K. Liu, C. J. Hill, S. B. Rafol, J. M. Mumolo, J. T. Trinh, M. Z. Tidrow and P. D. LeVan, "1024x1024 pixel MWIR and LWIR QWIP focal plane arrays and 320x256 MWIR:LWIR pixel colocated simultaneous dualband QWIP focal plane arrays,"

Proceedings of SPIE-Infrared Technology and Applications XXXI, vol. 5783, pp. 789-803, 2005.

[49] M. Jhabvala, D. Reuter, K. Choi, M. Sundaram, C. Jhabvala, A. La, A. Waczynski and J. Bundas, "The QWIP focal plane assembly for NASA's Landsat Data Continuity Mission," *Proceedings of SPIE-Infrared Technology and Applications XXXVI*, vol. 7660, p. 13, 2010.

[50] S. Crawford, R. Craig, A. Haining, J. Parsons, E. Costard, P. Bois, F. H. Gauthier and O. Cocle, "THALES long-wave advanced IR QWIP cameras," *Proceedings of SPIE-Infrared Technology and Applications XXXII*, p. 62060H, 2006.

[51] A. Majumdar, A. Shah, M. Gokhale, S. Sen, S. Ghosh, B. M. Arora and D. Tsui, "High-responsivity high-gain $In_{0.53}Ga_{0.47}As$-InP quantum-well infrared photodetectors grown using metal-organic vapor phase epitaxy," *IEEE Journal of Quantum Electronics,* vol. 41, no. 6, pp. 872-878, 2005.

[52] D. K. Sengupta, S. L. Jackson, A. P. Curtis, W. Fang, J. I. Malin, T. U. Horton, Q. Hartman, H. C. Kuo, S. Thomas, J. Miller, K. C. Hsieh, I. Adesida, S. L. Chuang, M. Feng, G. E. Stillman, Y. C. Chang, W. Wu, J. Tucker, H. Chen, J. M. Gibson and J. Mazumder, "Growth and characterization of n-type InP/InGaAs quantum well infrared photodetectors for response at 8.93 μm," *Journal of Electronic Materials*, vol. 26, pp. 1376-1381, 1997.

[53] J. Jiang, K. Mi, R. McClintock, M. Razeghi, G. Brown and C. Jelen, "Demonstration of 256 x 256 focal plane array based on Al-free GaInAs-InP QWIP," *IEEE Photonics Technology Letters,* vol. 15, no. 9, pp. 1273-1275, 2003.

[54] S. Ozer, O. Cellek and C. Besikci, "Assessment of large format InP/InGaAs quantum well infrared photodetector focal plane array," *Infrared Physics & Technology,* vol. 47, no. 1, pp. 115-118, 2005.

[55] S. Ozer, U. Tumkaya, B. Asici and C. Besikci, "Demonstration and Performance Assessment of Large Format InP–InGaAsP Quantum-Well Infrared Photodetector Focal Plane Array," *IEEE Journal of Quantum Electronics,* vol. 43, no. 8, pp. 709-713, 2007.

[56] S. U. Eker, Y. Arslan, A. E. Onuk and C. Besikci, "High Conversion Efficiency InP/InGaAs Strained Quantum Well Infrared Photodetector Focal Plane Array With 9.7 μm Cut-Off for High-Speed Thermal Imaging," *IEEE Journal of Quantum Electronics,* vol. 46, no. 2, pp. 164-168, 2010.

[57] C. Beşikci, S. V. Balcı, O. Tanış, O. O. Güngör and E. S. Arpaguş, "Grating-free high-x InP/InxGa1-xAs mid-wavelength infrared QWIP focal plane array," *Opto-Electronics Review,* vol. 31, p. e144563, 2023.

[58] S. D. Gunapala, S. V. Bandara, J. K. Liu, J. M. Mumolo, D. Z. Ting, C. J. Hill and J. Nguyen, "First demonstration of megapixel dual-band QWIP focal plane array," in *SENSORS, 2009 IEEE*, Christchurch, New Zealand, 2009.

[59] S. Bandara, S. Gunapala, J. Liu, S. Rafol, D. Ting, J. Mumolo, R. Chuang, T. Trinh, J. Liu, K. Choi, M. Jhabvala, J. Fastenau and W. Liu, "Four-band quantum well infrared photodetector array," *Infrared Physics & Technology,* vol. 44, no. 5, pp. 369-375, 2003.

[60] Y. Arslan, S. Eker, M. Kaldirim and C. Besikci, "Large format voltage tunable dual-band QWIP FPAs," *Infrared Physics & Technology,* vol. 52, no. 6, pp. 399-402, 2009.

[61] O. Cellek, S. Memis, U. Bostanci, S. Ozer and C. Besikci, "Gain and transient photoresponse of quantum well infrared photodetectors: a detailed ensemble Monte Carlo study," *Physica E: Low-dimensional Systems and Nanostructures,* vol. 24, no. 3, pp. 318-327, 2004.

[62] Y. Arslan, T. Çolakoglu, G. Torunoglu, O. Aktas and C. Besikci, "Enhanced performance QWIP FPAs," *Infrared Physics & Technology,* vol. 59, pp. 108-111, 2013.

[63] M. Z. Tidrow, K. K. Choi, A. J. DeAnni, W. H. Chang and S. P. Svensson, "Grating coupled multicolor quantum well infrared photodetectors," *Applied Physics Letters,* vol. 67, no. 13, pp. 1800-1802, 1995.

[64] I. Vurgaftman, J. R. Meyer and L. R. Ram-Mohan, "Band parameters for III–V compound semiconductors and their alloys," *Journal of Applied Physics,* vol. 89, no. 11, pp. 5815-5875, 2001.

[65] M. Levinshtein, S. Rumyantsev and M. Shur, Handbook Series on Semiconductor Parameters, World Scientific, 1996.

[66] H. Schneider, M. Walther, C. Schönbein, R. Rehm, J. Fleissner, W. Pletschen, J. Braunstein, P. Koidl, G. Weimann, J. Ziegler and W. Cabanski, "QWIP FPAs for high-performance thermal imaging," *Physica E: Low-dimensional Systems and Nanostructures,* vol. 7, no. 1, pp. 101-107, 2000.

[67] G. Karunasiri, J. S. Park, J. Chen, R. Shih, J. F. Scheihing and M. A. Dodd, "Normal incident InGaAs/GaAs multiple quantum well infrared detector using electron intersubband transitions," *Applied Physics Letters,* vol. 67, no. 18, pp. 2600-2602, 1997.

[68] R. Rehm, H. Schneider, M. Walther, P. Koidl and G. Weimann, "Avalanche multiplication due to impact ionization in quantum-well infrared photodetectors: A quantitative approach," *Applied Physics Letters,* vol. 82, no. 17, pp. 2907-2909, 2003.

[69] D. L. Perry and E. L. Dereniak, "Linear theory of nonuniformity correction in infrared staring sensors," *Optical Engineering,* vol. 32, no. 8, pp. 1854-1859, 1993.

[70] I. Ribet-Mohamed, J. Nghiem, M. C. Christol, M. Guénin, L. Höglund, E. Costard, J. Rodriguez and P. Christol, "Temporal stability and correctability of a MWIR T2SL focal plane array," *Infrared Physics & Technology,* vol. 96, pp. 145-150, 2019.

[71] F. Parra, P. Meza, C. Toro and S. Torres, "Infrared Focal Plane Array Imaging System Characterization by Means of a Blackbody Radiator," in *Progress in Pattern Recognition, Image Analysis, Computer Vision, and Applications*, Berlin, Heidelberg, 2011.

[72] K. K. Choi, D. P. Forrai, D. W. Endres and J. Sun, "Corrugated quantum-well infrared photodetector focal plane arrays," *IEEE Journal of Quantum Electronics,* vol. 45, no. 10, pp. 1255-1264, 2009.

[73] M. Kaldirim, Y. Arslan, S. U. Eker and C. Besikci, "Lattice-matched AlInAs–InGaAs mid-wavelength infrared QWIPs: characteristics and focal plane array performance," *Semiconductor Science and Technology,* vol. 23, no. 8, 2008.

[74] S. D. Gunapala, S. V. Bandara, J. K. Liu, C. J. Hill, S. B. Rafol, J. M. Mumolo, J. Thang, M. Z. Tidrow and P. D. LeVan, "MWIR & LWIR Megapixel QWIP focal plane arrays," *Infrared Systems and Photoelectronic Technology,* vol. 5563, pp. 141-148, 2004.

[75] H. Schneider, J. Fleissner, R. Rehm, M. Walther, W. Pletschen, P. Koidl, G. Weimann, J. Ziegler, R. Breiter and W. A. Cabanski, "High-resolution QWIP FPAs for the 8- to 12-μm and 3- to 5-μm regimes," *Proceedings of SPIE-Infrared Technology and Applications XXVIII,* vol. 4820, pp. 297-305, 2003.

[76] R. Breiter, J. Wendler, H. Lutz, S. Rutzinger, T. Schallenberg, J. Ziegler and I. Rühlich, "State-of-the-art MCT IR-modules with enhanced long term and cycle stability," *Proceedings of SPIE-Infrared Technology and Applications XXXVIII,* vol. 8353, p. 83532L, 2012.

[77] H. Yuan, G. Apgar, J. Kim, J. Laquindanum, V. Nalavade, P. Beer, J. Kimchi and T. Wong, "FPA development: from InGaAs, InSb, to HgCdTe," *Proceedings of SPIE-Infrared Technology and Applications XXXIV,* vol. 6940, p. 69403C, 2008.

[78] L. Höglund, S. Naureen, R. Ivanov, M. Pozzi, S. Almqvist, D. Rihtnesberg, S. Smuk, W. Diel, S. Fattala, A. Smuk, E. Trybom and E. Costard, "Type II superlattices: HOT MWIR production and development at IRnova," *Proceedings of SPIE-Infrared Technology and Applications XLV,* vol. 11002, p. 110020U, 2019.

[79] S. Eker, Y. Arslan and C.Beşikci, "High speed QWIP FPAs on InP substrates," *Infrared Physics & Technology,* vol. 54, no. 3, pp. 209-214, 2009.